Formation and Limiting Mechanisms for Very High Sea Surface Temperature: Linking the Dynamics and the Thermodynamics

DUANE E. WALISER

Institute for Terrestrial and Planetary Atmospheres, State University of New York at Stony Brook, Stony Brook, New York

(Manuscript received 2 December 1994, in final form 2 June 1995)

ABSTRACT

The present study composites atmosphere and ocean conditions associated with ocean hot spots. Ocean hot spots are defined as regions where SST exceeds 29.75°C and that have an area greater than 1×10^6 km^2. The composite atmosphere includes surface flux parameters, deep convection and cloud amounts, cloud radiative forcing, and analysis fields from the National Meteorological Center (NMC) and European Centre for Medium-Range Weather Forecasts weather forecasting systems. The composite ocean includes sea level height and the temperature and velocity structures down to 720 m from the NMC ocean forecasting system. These fields are composited for the months before, during, and after the appearance of hot spots in order to develop a four-dimensional picture of the atmosphere and ocean conditions that are associated with the formation and the decay of these very high ocean surface temperatures.

The analysis indicates that the formation of these hot spots is largely confined to the region within the 28°C isotherm of the long-term mean SST, with greatest concentrations occurring in the western Pacific warm pool. Extended analysis of the warm-pool hot spots (0°–10°S, 156°E–176°W) indicates strong influences from interannual, annual, and 30–60 day timescales, with La Niña conditions appearing to inhibit formation, southern summer favoring formation, and the descending (ascending) phase of the Madden–Julian oscillation (MJO) favoring formation (decay). This interaction with the MJO indicates how internal, or remotely forced, atmospheric variability, in addition to local feedbacks, may be playing a role to help limit SST. Furthermore, the out-of-phase relationship between SST and deep convection associated with this variability suggests the possibility of a positive feedback mechanism for the MJO. With respect to the surface heat budget, the data indicate that during the hot spot evolution, the convective perturbations to the surface shortwave exceed those for evaporation by at least a factor of 2.

The composite ocean conditions indicate that the rapidly varying atmospheric conditions associated with the hot spot evolution induce significant changes below the surface layer of the ocean as well. These changes appear to be primarily linked to the onset of westerly wind bursts associated with the enhanced deep convection. Removing the El Niño time periods from the composites indicates that the composite ocean is more dependent on the interannual state than the composite atmosphere. These results indicate that the ocean should not be rendered too simple with respect to understanding the limiting mechanisms of high SST.

1. Introduction

Great interest has surrounded the issue of climate changes associated with the observed anthropogenic increase in greenhouse gases (e.g., Manabe and Wetherald 1980; Somerville and Remer 1984; Schlesinger and Mitchell 1987; Cess et al. 1989; Lindzen 1990), particularly as it relates to implied or predicted changes in the earth's surface temperature. In response to this interest, and to improve our understanding of the coupling between the land, atmosphere, and ocean systems, significant attention has recently been directed toward understanding the mechanisms that act to provide an upper limit on surface temperatures in earth's present-day climate. Since the bulk of the earth's surface is covered by ocean and because the heat capacity of the oceans is so much greater than that of the land, a natural starting point is to first try to understand the mechanisms that provide the upper limit on sea surface temperatures (SSTs).

This topic was first directly addressed by Newell (1979) in a discussion of the relationship between global climate and the world's oceans.[1] Newell's approach was to balance a model tropical sea surface heat budget using a bulk aerodynamic formula to represent the behavior of the net longwave, evaporative, and sensible heat losses as functions of SST. To close the system, he further assumed the model tropical atmosphere

Corresponding author address: Dr. Duane E. Waliser, Institute for Terrestrial and Planetary Atmospheres, Marine Sciences Research Center, State University of New York at Stony Brook, Stony Brook, NY 11794-5000.

[1] In an earlier study, Priestly (1966) concluded that evaporative heat loss was the primary mechanism that curtailed the growth of temperatures over moist, vegetated land surfaces.

had clear skies and fixed values for air temperature (27°C), relative humidity (70%), and wind speed (3 m s^{-1}). The resulting heat budget balanced at about 30°–31°C and as expected was largely a balance between incoming solar radiation and outgoing latent heat loss, with evaporation increasing rapidly with SST (see his Fig. 5). This prompted Newell to conclude that evaporation was the primary mechanism that limited climatological SSTs to about 30°C.

A modification to Newell's conclusion was made by Graham and Barnett (1987) on the basis of their analysis of the relationship between large-scale tropical deep convection and SST. They found a fairly rapid increase in the intensity/frequency of deep convection with SST in the range of about 26°–28°C that was fairly widespread over the global tropical oceans (cf. Krueger and Gray 1969; Gagdil et al. 1984). The ubiquitous cloudiness generally associated with tropical deep convection prompted them to modify the simplified model of Newell to account for the cloudiness bound to be present at such warm SSTs. They assumed that the effect of these cloud systems would result in a mean albedo of about 30% and thus reduce the incoming solar radiation in Newell's model to a degree that the surface energy budget balanced at about 28°C. This temperature coincided with the peak in their observed population distribution of SST. From these results, they concluded that cloud cover in addition to evaporative cooling placed an upper limit on SST.

Significantly more attention turned to the issue after Ramanathan and Collins (1991, hereafter referred to as RC) hypothesized that solar shielding due to highly reflective cirrus clouds was the primary limiting mechanism on SST growth and therefore acted as a "thermostat" for the warmest tropical regions. Their hypothesis was based on three premises. First, observations and model calculations show that the downward longwave emission from the atmosphere to the surface begins to grow at a faster rate than the upward longwave emission from the surface in the range of SST greater than about 25°C. This is primarily due to increased concentrations of, and enhanced radiation trapping effects from, atmospheric water vapor (Raval and Ramanathan 1989; Stephens and Greenwald 1991). This phenomena is often referred to as the "super greenhouse effect" and results in the longwave radiation component ceasing to function as a negative feedback on SST growth in the upper range of tropical SSTs. Second, RC found that local changes in top-of-the-atmosphere, shortwave cloud forcing occurring in association with tropical Pacific SST changes during the 1985–87 El Niño–Southern Oscillation (ENSO) "cycle" indicated cloudiness could act as a negative feedback with a magnitude of about -22 W m^{-2} K^{-1}. Third, RC argued that surface evaporation could not function as a limiting mechanism in the warmest oceans because evaporation adds moisture to the atmospheric column and thus enhances the super greenhouse effect. RC also note that water vapor is actually imported into the warmest ocean regions and that evaporation tends to be low in these areas. Given these facts and inferences, RC concluded that SST-induced changes in highly reflective cirrus clouds (mainly thick cirrostratus anvils) accounted for the negative feedback, which limited SSTs to about 30°–32°C.

Following the "thermostat hypothesis" were many studies that questioned it, or its range of applicability, generally based on one or both of RC's latter two premises. Most often critics argued 1) that surface evaporation acts as the primary limiting mechanism and/or 2) that SSTs are coupled to cloudiness mainly through large-scale dynamics, and therefore elements of the three-dimensional circulation play a more important role than is implied in RC's hypothesis. These studies took many forms, including heuristic arguments (Wallace 1992), inferences from satellite data (e.g., Fu et al. 1992; Arking and Ziskin 1994; Liu et al. 1994), simplified model approaches (Hartmann and Michelsen 1993), and numerical model simulations (Lau et al. 1994; Waliser et al. 1994). It is important to keep in mind that in some of the studies above, part of their conclusions related to the thermostat hypothesis are actually directed toward the regulating mechanisms of the ENSO cycle and not necessarily the mechanisms that limit the maximum SST. For example, both the Fu et al. and Hartman and Michelson studies show that ENSO-related changes in basin-averaged evaporation over the Pacific can be significant, while basin-averaged changes in shortwave cloud forcing (or its proxy) are negligible. Similarly, Waliser et al. showed, using forced and coupled numerical model simulations, that SST-induced cloud shortwave feedbacks do not appear to be critical to the first-order regulation of the ENSO phenomena.

Waliser and Graham (1993, hereafter WG) examined the implications of the local relationship between large-scale deep convection and SST in the regime of very warm SST. With the advent of significantly more data than was used in the Graham and Barnett study, Waliser et al. (1993) resolved the high SST limit of the relationship (SST > 29°C). They found that above about 29.5°C the intensity/frequency of monthly averaged deep convection decreases with increasing SST, and thus the highest observed SSTs tend to be found in areas or at times of suppressed deep convection. From this result, along with the finding that suppressed (enhanced) deep convection tends to be associated with positive (negative) rates of SST change, WG concluded that 1) when deep convection is suppressed in warm-pool regions by atmospheric variability uncoupled to the local SST, areas of very warm SST (>30°C) can form and 2) these high SSTs are unstable and lead to probable increases in deep convection that cool the SST through enhanced cloudiness and turbulent heat exchange. Waliser and Graham also attempted to address whether the convective perturbations to the sur-

face shortwave or latent heat fluxes were larger and concluded from limited data and a simplified surface heat budget model that the cloud-shielding effect on shortwave radiation appeared to dominate.

The above studies have focused a significant amount of attention and effort onto the question of SST limiting mechanisms, have led to some useful paradigms for its consideration, and have led to some important and useful advances in our understanding of tropical air–sea interactions. However, there still remain deficiencies in their content as a whole. First, virtually all the above studies ignore ocean processes, at least as far as providing analysis of data or modeling its behavior. Second, many of the studies have limited applicability because their conclusions were based on the analysis of local relationships (e.g., RC, WG, Arking and Ziskin) and therefore large-scale coupling and remote forcing issues are not directly addressed. Meanwhile, the studies that do invoke the response/influence of the large-scale circulation rely on little or no observed data concerning the actual circulation but instead rely on simple arguments, models, or proxy data such as satellite cloudiness or radiation data (e.g., Wallace, Fu et al., WG, Hartman and Michelson). Third, as with any study based on observations, many of the above have limited applicability due to the amount, accuracy, and sampling of the data used. Fortunately, the datasets obtained by the recent Tropical Oceans and Global Atmosphere Coupled Ocean–Atmosphere Research Experiment (TOGA COARE) (1991) and Central Equatorial Pacific Experiment (CEPEX) (1992) field programs will help address some of these deficiencies.

The present study of very warm SST and its limiting mechanisms is an attempt to overcome some of the above shortcomings by 1) considering aspects of the ocean state and its circulation, 2) retaining the three-dimensional character of the data in the analysis, and 3) incorporating as much applicable "data" as possible from as many "platforms" as possible from the time period 1970 to 1992 in order to reduce the reliance on any one time period or dataset. The goal is to build a comprehensive picture of the four-dimensional atmosphere and ocean conditions associated with the formation and decay of very high SST. Specific objectives of the analysis are as follows:

- determine the spatial and temporal variability of very high tropical SST
- investigate the mechanisms leading to suppressed convective conditions, and thus the formation of very high SST
- assess the relative roles of evaporation versus cloud forcing in limiting SST
- examine the coupling between local and remote forcing in both the production and the subsequent cooling of high SST
- examine the evolution of the near-surface ocean circulation during the formation and decay of very high SST.

The method involves compositing ocean and atmosphere conditions from 30°N to 30°S using monthly data based on a specific SST selection criteria: the occurrence of a widespread region of very high SST or ocean "hot spot." Composites are produced for the month(s) before, during, and after the occurrences of these hot spots. Large-scale compositing is employed in order to capture the basin-to-global-scale conditions, as well as the local processes, that may be significant to the formation/decay of areas of very high SST. In the next section the data sources used in this study are described. Section 3 discusses the method of analysis, including the definition of an ocean hot spot. Section 4 presents the results. Section 5 concludes with a summary and discussion.

2. Data

Data for this study comes from a wide range of sources. Each of the datasets used were provided in a gridded format of monthly values, and each dataset's native grid format and resolution were retained in the analysis. Monthly values were used throughout the study and anomalies are taken about the annual cycle. The annual cycle for each dataset was computed from each dataset's entire length. Figure 1 shows the temporal coverage for each of the datasets used in this study. The solid black lines indicate in-situ-based data, the dark gray lines indicate satellite-based data, and the light gray lines indicate model analysis fields.

The in-situ-based data consists of SST, Coupled Ocean–Atmosphere Data Set (COADS), and The Florida State University (FSU) wind stress product. The SST is from the Climate Analysis Center and combines an in situ measurement analysis from 1970 to 1981 with a blended analysis of satellite-derived and in situ measurements from 1982 to 1992, each produced monthly on a global 2° × 2° grid (Reynolds 1988). The COADS (1985) dataset is made up of the monthly summaries trimmed product from 1970 to 1992, which is produced on a global 2° × 2° grid. It is used here to estimate variability in air–sea humidity difference and air–sea humidity difference multiplied by the local wind speed for the purposes of diagnosing variability in surface latent heat flux. Surface wind stress and wind speed fields were obtained from the FSU monthly surface wind analysis. The output from this analysis is in the form of a pseudostress on a 2° × 2° grid. The Indian Ocean analysis is by Legler et al. (1989), and the Pacific Ocean analysis is by Shriver and O'Brien (1993).

The satellite-based data includes the highly reflective clouds (HRC) and outgoing longwave radiation (OLR) datasets, products from the International Satellite Cloud Climatology Project (ISCCP) and Earth Radiation Budget Experiment (ERBE) datasets, along with products derived from the ISCCP dataset and the Microwave Sounding Unit (MSU) sensor.

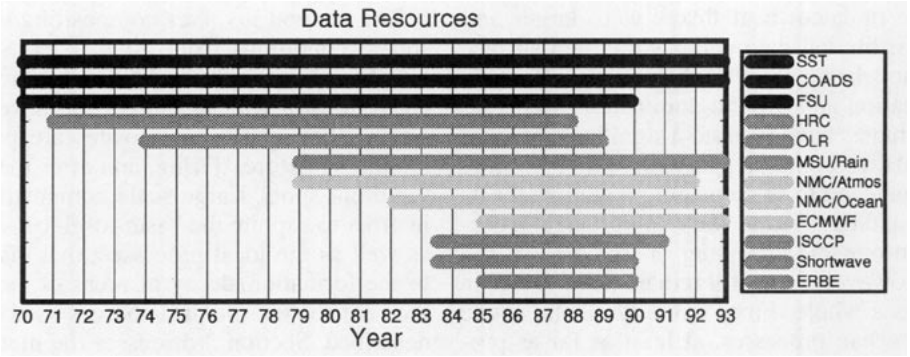

FIG. 1. Temporal coverage of the datasets used in this study. Solid black lines indicate in-situ-based data, dark gray lines indicate satellite-based data, and light gray lines indicate model analysis fields. See descriptions in section 2.

This ISCCP stage C2 dataset (Rossow and Schiffer 1991) contains monthly averages of derived cloud types in terms of their frequency of occurrence, cloud-top temperatures, and cloud-top pressures, along with other auxiliary information and data products at 2.5° resolution. All derived cloud types are based on cloud-top pressure and optical thickness and are mutually exclusive. For example, the deep convective cloud type has been assigned to observations that have an optical thickness greater than 23 and cloud-top pressure less than 440 mb. This classification indicates very deep (or thick) clouds with high cloud tops. The individual classifications are assigned from daytime observations only and have a sampling interval of 3 h. The specific C2 data examined in this study are the frequencies of the high cloud types: deep convective, cirrostratus, cirrus. The data used in this study extends from July 1983 to December 1990.

The monthly HRC (Garcia 1985) dataset is derived from a daily, binary indicator of the presence of organized deep convection based on the subjective analysis of visible and infrared satellite mosaics (daytime only). The infrared data is used as a proxy for cloud-top height, and thus to indicate the presence of high cloud tops, specifically convective systems. The visible information is used to exclude the large-scale cirrus clouds associated with convective systems. The results from this analysis are combined in the form of binary-valued, daily "images" with 1° spatial resolution that indicate regions where large-scale convection is present between 25°N and 25°S and the years 1971 to 1987. These daily images were then combined to form monthly values on a 2° × 2° grid, for example, days per month deep convection was present at each grid point. In the sense that bright, high clouds are designated as HRC, this method is a subjective analog to the objective approach used in defining ISCCP deep convective clouds. The HRC has been shown to agree fairly well with the ISCCP C2 deep convective index, particularly in the deep Tropics (Waliser et al. 1993).

The OLR dataset was constructed by Horel and Cornejo-Garrido (1986) from daytime and nighttime archived OLR estimations (in W m^{-2}), interpolated onto a 2° × 2° grid between 30°N and 30°S for the global Tropics, and then time averaged into 5-day means; these were subsequently averaged in monthly values. The dataset used in this study extends from June 1974 to May 1988 with gaps of 10 months during 1978 and 2 months during 1987. OLR is an estimate of the total outgoing longwave radiation at the top of the atmosphere inferred from multiband satellite radiation measurements (Gruber and Krueger 1984). It has been used in many studies as an indicator of cloudiness over the tropical oceans, particularly deep convective systems (e.g., Liebmann and Hartmann 1982; Rasmusson and Wallace 1983; Graham and Barnett 1987; Lau and Chan 1985).

The downwelling surface shortwave radiation is a satellite-derived product based on the method of Gautier et al. (1980) using the ISCCP stage C1 data. The shortwave data is provided monthly on a global 2.5° × 2.5° grid from July 1984 to December 1989 (Wang 1994). ERBE data was used to obtained top-of-the-atmosphere shortwave and longwave cloud-forcing values (R. D. Cess 1994, personal communication). ERBE data extends from 1985 to 1989 and is provided on a 2.5° × 2.5° grid. The ocean rainfall estimates were derived by Spencer (1993) using the MSU channels 1, 2, and 3. Rain rate is diagnosed when cloud water and rainwater induced radiometric warming of the channel 1 brightness temperatures exceeds a cumulative frequency distribution threshold of 15% after correction for airmass temperature determined from the channel 2 and 3 measurements. The monthly dataset used here is produced on a global 2.5° × 2.5° grid and extends between 1979 and 1991.

The model analysis fields include products from the forecasting systems of both the National Meteorological Center (NMC) and the European Center for Medium-Range Weather Forecasts (ECMWF). NMC's

monthly analysis product was used for the years 1979 and 1991. The data are provided on a global 2.5° × 2.5° grid. Zonal, meridional, and vertical velocities, along with temperature, were used in this study. Relative and specific humidity were obtained from the ECMWF monthly analysis for the years 1985 to 1991 (K. E. Trenberth 1994, personal communication). For details on the changes made to these assimulation systems over most of the study period, see Trenberth and Olson (1988). Three-dimensional ocean data were obtained from the NMC ocean analysis system (Ji et al. 1995). This ocean reanalysis begins in February 1982 and extends to the present and incorporates only thermal data in the way of sea surface temperatures, ship of opportunity expendable bathythermographs (XBT), and TOGA Tropical Atmosphere–Ocean (TAO) array data (Hayes et al. 1991; McPhaden 1993). The model analysis is provided for the tropical Pacific, from 35°S to 45°N, 122.25°E to 71.25°W on a 1° × 1.5° (lat × long) grid. Zonal and meridional wind stress and currents, along with temperature and (diagnostic) sea level displacement, were used for this study. Salinity was not analyzed since observed freshwater fluxes are not specified in the assimulation procedure.

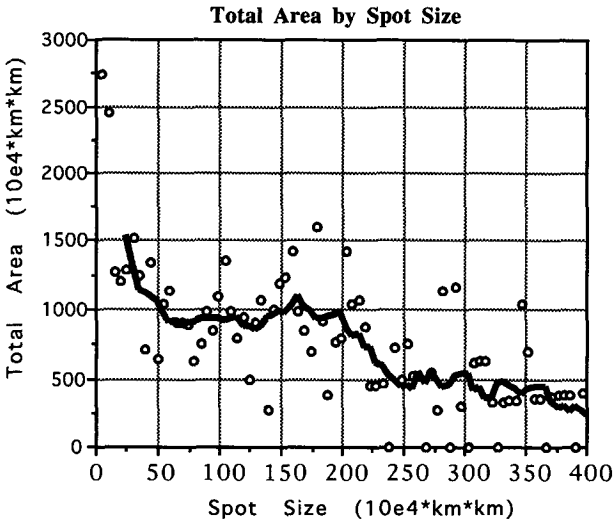

FIG. 2. Histogram of total area accounted for by each size hot spot in the SST record meeting the SST threshold criteria (>29.75°C; see section 3). This histogram was produced by multiplying the number of hot spots found for a given size times their area coverage. Dividing the spot size value (x axis) by 5 gives the approximate number of 2° × 2° SST pixels making up the hot spot. The solid line represents a 9-point box average of the individual points.

3. Methods

The analysis procedure can be broken down into two parts: 1) identify occurrences of very warm sea surface temperature, or "hot spots," in the SST record, and 2) composite the geophysical conditions associated with the evolution of these hot spots.

a. Hot spot identification

The initial step was to identify an SST threshold to use for the identification of ocean "hot spots." The threshold was taken to be 29.75°C for two reasons. First, this temperature comes very close to representing an upper bound for climatological SST values from monthly data for the tropical oceans. Second, it is also near the lower limit of the regime where deep convection tends to decrease with increasing SST (Waliser et al. 1993). The next step was to use this threshold to identify and characterize "hot spots" in the SST record. This was done by setting all grid points with SST less than the threshold value to a "missing" value. Then each SST monthly map was analyzed using a recursive searching algorithm to identify each individual, self-contained region of high SST. Each region was characterized by its 1) month of occurrence, 2) SST-weighted mean latitude and longitude, 3) spatial area, and 4) mean SST value. Figure 2 shows the total area of ocean surface with temperature greater than or equal to 29.75°C that is accounted for by each size spot. This figure was obtained by multiplying the number of occurrences of each size hot spot by the spot area. It indicates that besides the preference for small spot sizes, owing to the relatively small deformation scale of the ocean and the many landlocked or near-landlocked regions, such as the Red Sea, there is a slight preference for these spots to occur with a size on the order of 1.5 × 10^6 km^2. This latter size corresponds more closely to the square of the deformation scale of the atmosphere rather than the ocean and indicates the key role the atmosphere plays in helping to form these ocean hot spots. To include only hot spots that are most likely linked to large-scale atmospheric forcing, a threshold of 1.0 × 10^6 km^2 was chosen as a minimum size for an ocean hot spot. Thus, a hot spot in this study is defined as a self-contained, connected region with SST greater than or equal to 29.75°C and a minimum area of 1.0 × 10^6 km^2.

Figure 3 shows a map of the 258 hot spot locations that were extracted from the SST record using the above procedures and criteria. As expected, the greatest concentration of hot spots is in the western Pacific warm-pool region. Other high-concentration regions tend to be associated with monsoon regions, such as the north Indian Ocean and off the northern coast of Australia and the southern coast of Central America. Additionally, there are a number of hot spots occurring in the open ocean region of the northern tropical Pacific.

b. Compositing procedure

Compositing is performed as follows: for each hot spot occurring in the tropical western Pacific region 0°–10°S, 156°E–176°W, hereafter referred to as the

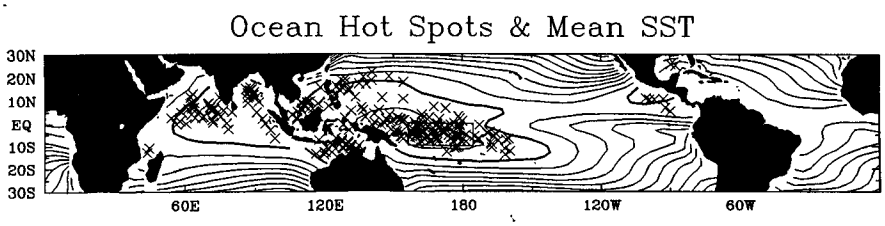

FIG. 3. Map showing all hot spots in the SST record meeting both the SST threshold criteria (>29.75°C) and the size criteria (>10^6 km^2; see section 3). Contours are every 1°C with the thick contour line representing the 28°C contour. In this study, ocean and atmosphere conditions are composited for the hot spots that occur in the rectangular "selection" region (0°–10°S and 156°E–176°W).

"selection region," the corresponding monthly and monthly anomaly data between 30°N and 30°S for all the ocean and atmospheric variables, if and where available (see section 2 and Fig. 1), are extracted and averaged. These averages are referred to as month = 0 conditions. To obtain a description of the temporal evolution of these ocean hot spots, the conditions for the months before and after the occurrence of the hot spot are also extracted and averaged. These averages are referred to as month = 1 and month = +1 conditions, respectively. If a hot spot lasted more than one month, that is, a hot spot occurred two months in a row in the selection region, then each occurrence is averaged into the month = 0 conditions and the month before (after) the first (last) hot spot are averaged into the month = 1 (+1) conditions. Given the varying time periods of the datasets used in this study, this method of compositing will not always average exactly the same months for all variables. For example, the composite SST anomaly is made up of hot spots that occur between 1970 and 1991, while the composite 200-mb wind, for example, is made of up of conditions with hot spots between 1979 and 1991.

4. Results

a. Temporal variability

Figure 4a is a scatter diagram showing the size and the month of occurrence for the ocean hot spots that formed in the global tropical oceans (open) and in the selection region (filled). This diagram shows that there is a fairly pronounced interannual signature in the development of these ocean hot spots, particularly those with very large area. Especially evident are the impacts from the La Niñas of 1974–76, 1985, and 1988–89, which appear to reduce the number and size of hot spot occurrences during those relatively cold ENSO phases.[2] Figure 4b is a histogram showing the calendar months in which the hot spots occurred for both the global tropical oceans (gray) and the selection region (black). The histogram shows an obvious impact from the annual cycle in the development of the ocean hot spots. Southern Hemisphere summer is a favored time for hot spot development in the selection region, while globally, the months of April and May are preferred. These global tendencies are most strongly influenced by the preferred development of hot spots in the Indian Ocean and the South China Sea prior to the onset of the summer monsoon. Figure 4c is a histogram showing the number of times a hot spot persisting for a given number of months occurred in the selection region. The histogram indicates that the hot spots forming in the selection region have a typical lifetime of about one month, with several lasting two to three months, and a few lasting up to several months.[3] These temporal characteristics emphasize the significant role that multiple timescales (interannual, annual, and monthly) have in the formation and decay of very warm SST in the western Pacific warm pool.

b. SST and deep convection

Figure 5 shows the evolution of the large-scale, composite, anomalous SST pattern associated with the ocean hot spots occurring in the western Pacific selection region (i.e., those in the rectangle of Fig. 3 and the filled markers/bars in Figs. 4a,b). The three panels (a,b,c) show the month = −1, month = 0, and month = +1 composites from top to bottom, respectively. Shown to the right of each map is the number of monthly observations in each composite's average. The selection region is plotted on each composite to facilitate comparisons of the different fields in the region of greatest SST changes. The basin-scale pattern is similar during each of the three phases of evolution (i.e., month = −1, 0, + 1) and appears to be consistent with a weak ENSO warm phase (e.g., Philander 1991),

[2] The fact that the SST record was only based on in situ data prior to 1982, and therefore did not have the virtue of satellite coverage, could play a role in the overall diminished number of hot spots appearing in the SST record during the 1970s.

[3] The No El Niño case in Fig. 4c (light bars) will be discussed in section 4f.

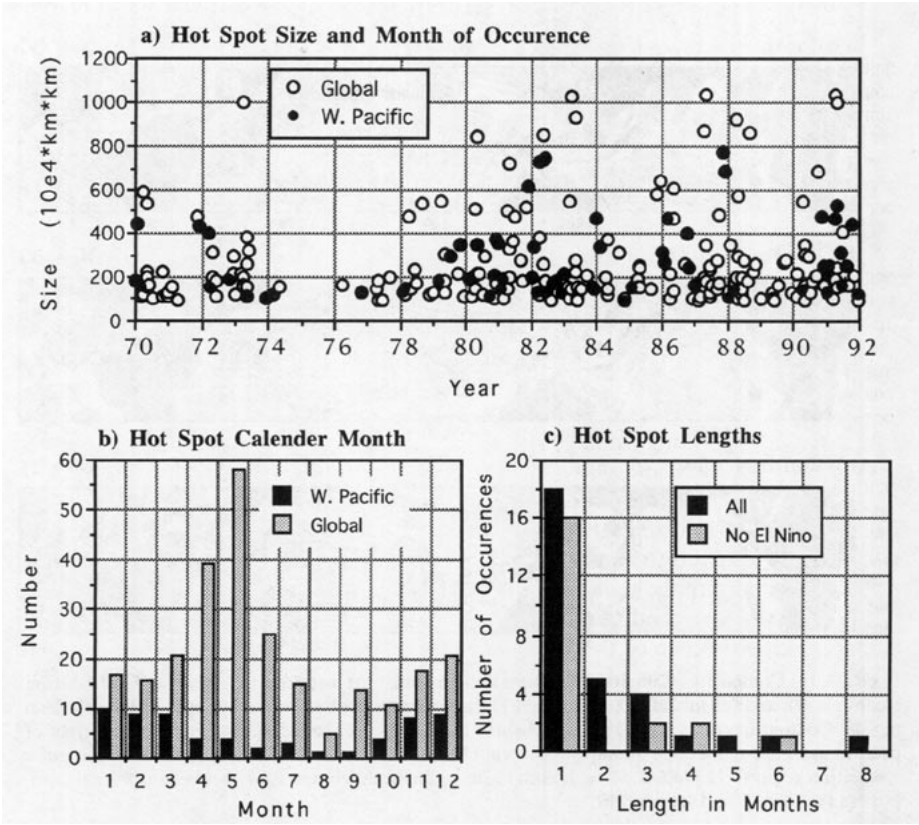

FIG. 4. (a) Scatter diagram showing the size and the month of occurrence for all ocean hot spots (open) and those occurring in the selection region (0°–10°S, 156°E–176°W). (b) Histogram showing calendar month of occurrence for hot spots shown in (a). (c) Histogram showing the number of hot spots persisting for a given number of months in the selection region (black bars). Gray bars are for all hot spots excluding those occurring in low Southern Oscillation (SO) index periods (see section 4f).

which in turn is loosely consistent with the scatter diagram in Fig. 4a. This aspect of the composites, that is, their relationship to ENSO, will be examined further in section 4f. As expected, the most apparent variation in the SST during the three "months" is near the selection region where the SST anomaly rises from about 0.1°C during month = −1 to a maximum value of about 0.6°C during month = 0, and then cools back to about −0.1°C. Data are presented in appendix A that illustrate the degree that these composite-to-composite changes in SST (as well as the changes for many other quantities discussed below) averaged over the selection region are statistically significant. Note that the histogram shown in Fig. 4b indicates that the corresponding composite total SST, or any other total field (not shown), would be most consistent with a Southern Hemisphere summer (December–February) pattern.

Figure 6 shows the evolution of anomalous HRC and thus the large-scale deep convection pattern. In the month = −1 composite, before the development of the hot spot, there is anomalous positive deep convection in the central and western Pacific, over the African and South American landmasses, and the western Indian Ocean. However, during the month(s) the hot spot occurs (month = 0), much of this convection is suppressed with slight positive anomalies occurring only over parts of Africa and South America and the eastern Indian Ocean. Finally, during the month after the occurrence of the hot spot (month = +1) there is a very large positive anomaly of deep convection located directly over what was the ocean hot spot, an HRC anomaly that is about 30%–50% of the climatological value during this time period (i.e., 3–6 days mo^{-1}: Garcia 1985; Waliser and Gautier 1993), which as mentioned above, corresponds most closely with Southern Hemisphere summer. The evolution of the MSU-derived rainfall (not shown) is consistent with the HRC evolution shown in Fig. 5. The positive HRC anomalies before and after the occurrence of the hot spot are associated with rainfall anomalies of about +60 and +85 mm mo^{-1}, respectively. The suppression of deep convection occurring in the selection region during the occurrence of the hot spot is associated with about a −30 mm mo^{-1} anomaly. The negative anomalies in convection occurring in the eastern

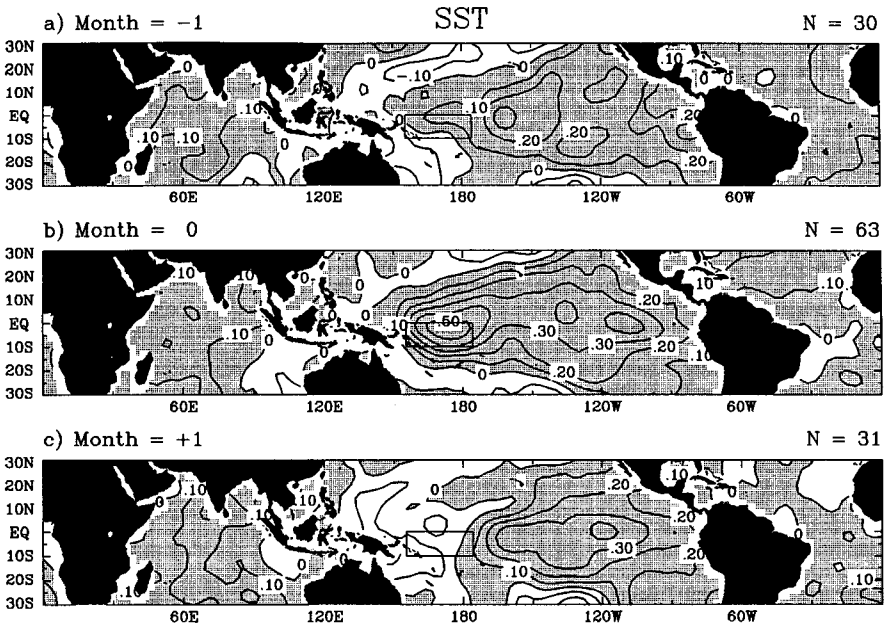

FIG. 5. (a) Composite anomalous SST for all the months: (a) just prior to (month = 1), (b) during (month = 0), and (c) just after (month = +1) the occurrence of an ocean hot spot in the selection region. Contour intervals are 0.1°C, and positive anomalies are shaded. Shown in the upper right of each map is the number of monthly observations in each composite's average. The rectangular "selection region" is plotted on each composite to facilitate comparisons between different composites (see Fig. 3 and section 3b).

Indian Ocean during the month = ±1 composites are also associated with rainfall anomalies of about −30 mm mo^{-1}.

There are three aspects in the above composites that are particularly interesting to consider. First, the HRC anomalies appear to be organized on a very large scale.

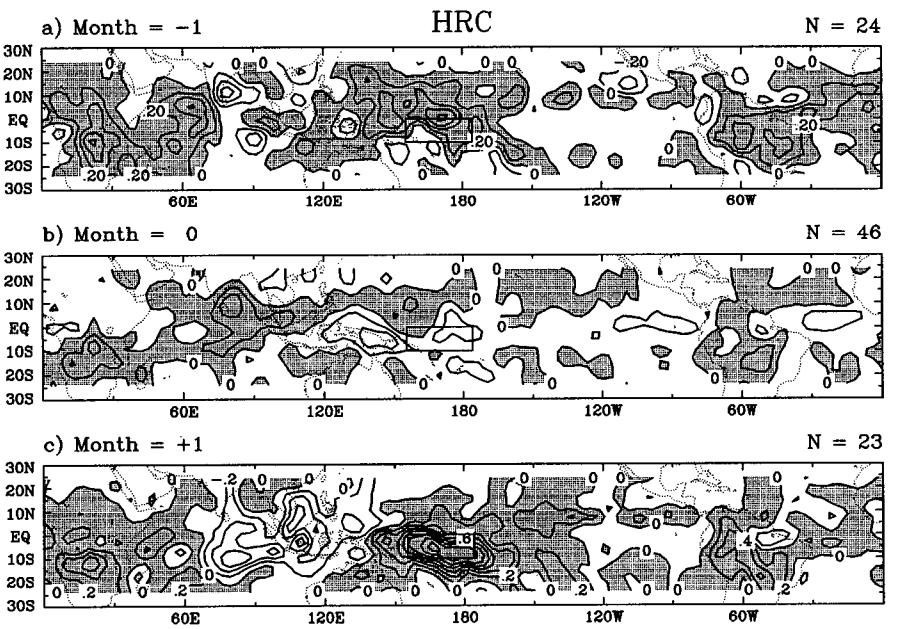

FIG. 6. Same as Fig. 5 except for HRC; contour intervals are 0.2 days mo^{-1}.

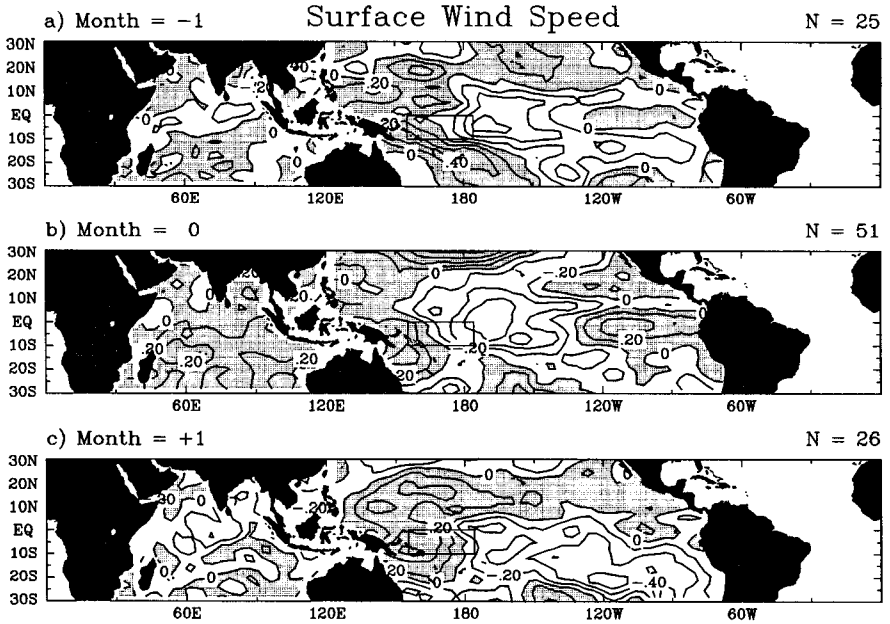

FIG. 7. Same as Fig. 5 except for surface wind speed; contour intervals are 0.2 m s^{-1}.

These global-scale patterns, along with the timescales implied by Fig. 4c, suggest a link between the formation/decay of these ocean hot spots and the 30–60 day, or Madden–Julian, oscillation (Madden and Julian 1971; Weickman 1983; Emanuel 1987; Lau and Chan 1988; Neelin and Yu 1993; Salby and Hendon 1994; Hendon and Salby 1994). This link will be further investigated in sections 4d and 5. Second, the SST and deep convection anomalies tend to be out of phase (i.e., 180°) in the selection region. This out-of-phase relationship is consistent with the local relationship between very high SST (>29.5°C) and deep convection discussed in the introduction where the inferences were 1) deep convection overall acts to cool the ocean surface, 2) suppressing deep convection leads to very warm, unstable, SSTs, and 3) any ensuing convection will damp the SST back to "equilibrium" values. Third, does the enhanced precipitation over the selection occurring in the month = −1 composite impact the surface mixed layer enough to predispose it to enhanced warming during the month = 0 composite? The next two sections are meant to address two questions concerning the first two of these inferences. First, what is the relative strength of the convective perturbations to the dominant heat flux terms that lead to the surface heating and cooling? Second, what mechanisms lead to the suppressed (enhanced) convective conditions that are associated with the warm (cool) SSTs? The latter question, concerning the role of the freshwater flux on the surface mixed layer, is beyond the scope of this study given the lack of data available to address this issue.

c. *Surface fluxes and cloudiness*

As stated above and in the introduction, one of the objectives of this study is to determine the components of the ocean–atmosphere system that lead to hot spot formation and decay. Those processes responsible for the decay phase are the processes that most likely play dominant roles in regulating and limiting tropical SSTs. Figures 7, 8, and 9 present the composite evolution of the surface wind speed, surface minus near-surface specific humidity difference, $(Qs - Qa)$, and $(Qs - Qa)$ times surface wind speed, $(Qs - Qa)W$. The latter represents a proxy for the surface latent heat flux. Figures A1c and A1d indicate the statistical significance of the composite to composite changes averaged over the selection region. Figure 7 indicates modest changes occurring in the spatial structure of the surface wind speed anomaly in the selection region. In each of the three phases, the wind anomaly is negative in the eastern part of the selection region and positive in the western part. During the warm month (month = 0), the negative anomaly, which extends eastward from the selection region into the central Pacific, has its largest magnitude and spatial coverage (about −0.5 m s^{-1}). In the month = +1 composite, the area and the magnitude of this negative anomaly is curtailed in favor of much stronger positive wind anomalies (about 0.5 m s^{-1}) over the western part of selection region, extending over most of the northern tropical western Pacific. Note these changes in anomalous wind speed are occurring in an area where the climatology is about 3–4 m s^{-1}. As will be evident in the 850-mb wind field

shown in section 4d, these changes in wind speed structure in and near the selection region appear to be associated with the development of "westerly wind bursts" linked to the enhanced deep convection occurring during this phase.

Figure 8 shows the evolution of the specific humidity difference ($Qs - Qa$). Most apparent is the positive anomaly, as great as 0.5 g_w kg_a^{-1}, in the month = 0 composite in the selection region, where mean values are about 6 g_w kg_a^{-1}. This ($Qs - Qa$) anomaly is less than would be expected if Qa was assumed constant and the SST changed in accordance with Fig. 5. In this case, Qs would change by about 0.9 g_w kg^{-1} (for SST change of 0.6°C). Therefore, there is a corresponding increase in Qa as well of about 0.4 g_w kg^{-1}. Comparing Figs. 7 and 8 shows that this positive ($Qs - Qa$) anomaly is nearly collocated with the broadened negative wind speed anomaly; thus, we might expect much of a net change in the evaporation in this area. Moreover, the enhanced structure of positive wind speed anomalies in the western portion of the selection region in the month +1 composite are not associated with any significant anomalies in ($Qs - Qa$), and thus we might not expect to see dramatic changes in the surface latent heat flux.

Figure 9 shows the evolution of the specific humidity difference times the local wind speed [$(Qs - Qa)W$; the average of the products, not the product of the averages]. While this is a very noisy field with very little coherent structure, the figure suggests that the slightly lower wind speeds and higher ($Qs - Qa$) values in the month = 0 composite end up offsetting each other, resulting in almost no $(Qs - Qa)W$ anomaly during the occurrence of the hot spot. In the month = +1 composite, the higher (lower) wind speeds in the central/western (eastern) portion of the selection region appear to produce $(Qs - Qa)W$ anomalies of the same sign with magnitudes of about ±2 g_w m kg_a^{-1} s^{-1} (mean values are about 30 g_w kg_a^{-1}). The magnitude of the surface evaporation anomalies can be estimated by using the bulk aerodynamic formula [$L\rho C_E(Qs - Qa)W$, where $L = 2.5$ J kg_w^{-1}] by assuming values for the near-surface air density ($\rho \sim 1.2$ kg_a m^{-3}) and exchange coefficient ($C_E \sim 1-2 \times 10^{-3}$). Multiplying the peak $(Qs - Qa)W$ anomalies in the selection region of Fig. 9c by the quantity ($L\rho C_E = 3-6 \times 10^3$ J kg_a kg_w^{-1} m^{-3}) gives an estimate of monthly evaporation anomalies of between ±3 and 12 W m^{-2}. While these perturbations magnitudes are consistent with the averaged effects due to disturbed versus undisturbed conditions found in the western Pacific by Young et al. (1992), the significance levels presented in appendix A indicate that these composite-to-composite changes averaged over the selection region (Fig. A1c) do not represent statistically significant changes owing to the high variance and poor sampling of the $(Qs - Qa)W$ quantity.

The other important component of the surface energy budget to most likely undergo significant perturbations is the downwelling surface shortwave radiation (SW). Figure 10 shows the evolution of the anomalous SW. From the maps of HRC evolution in Fig. 6, we would expect enhanced SW during the month(s) of the hot

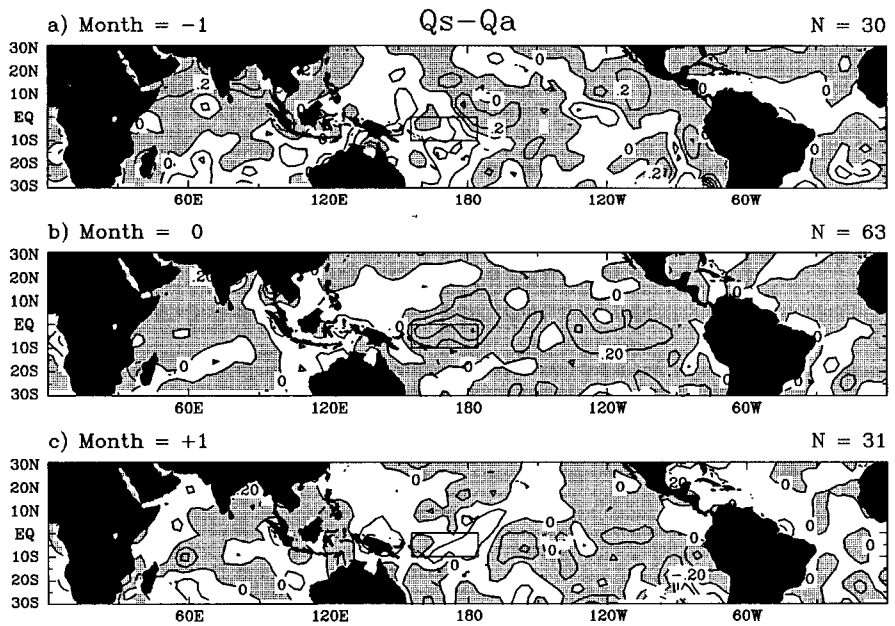

FIG. 8. Same as Fig. 5 except for $Qs - Qa$; contour intervals are 0.2 g_w kg_a^{-1}. The number of monthly observations (N) in this case only represents those locations that are sampled every month in the COADS data.

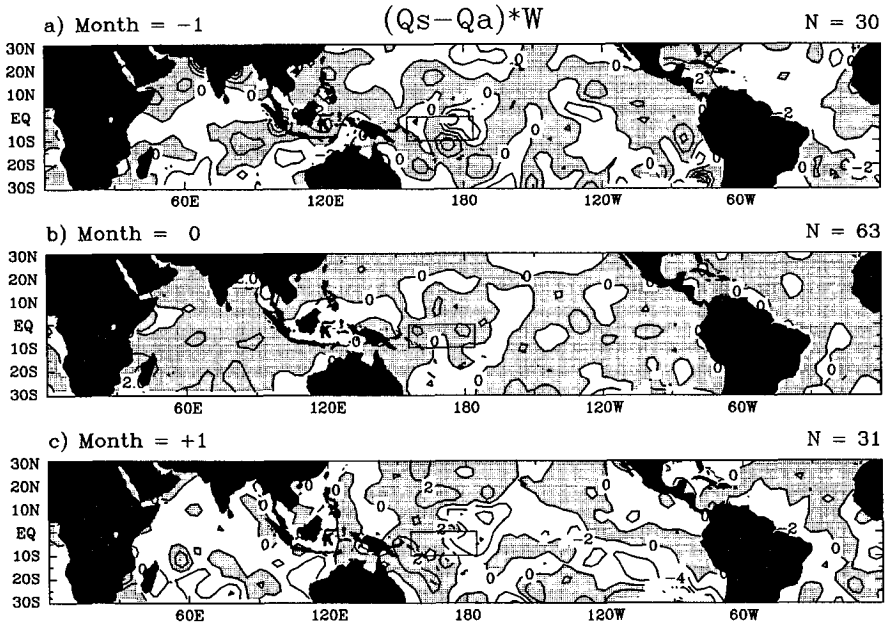

FIG. 9. Same as Fig. 8 except for $(Qs - Qa)W$; contour intervals are 2 g_w m kg_a^{-1} s^{-1}.

spot, when convection is suppressed, and decreased SW before and after the occurrence of the hot spot, particularly in the month = +1 composite. As the diagram indicates, the selection region experiences slight enhancements of downwelling SW, of only a few W m^{-2}, over about two-thirds of the domain, and reduced shortwave in the northern branch of the intertropical convergence zone (ITCZ). Note that the SW dataset covers a different time period than the HRC and therefore is compositing over a different set of hot spot occurrences (see ISCCP discussion below). Consistent with our expectations, the monthly averaged SW is reduced in the month = +1 composite over most of the selection region by up to 25 W m^{-2}. This figure is also

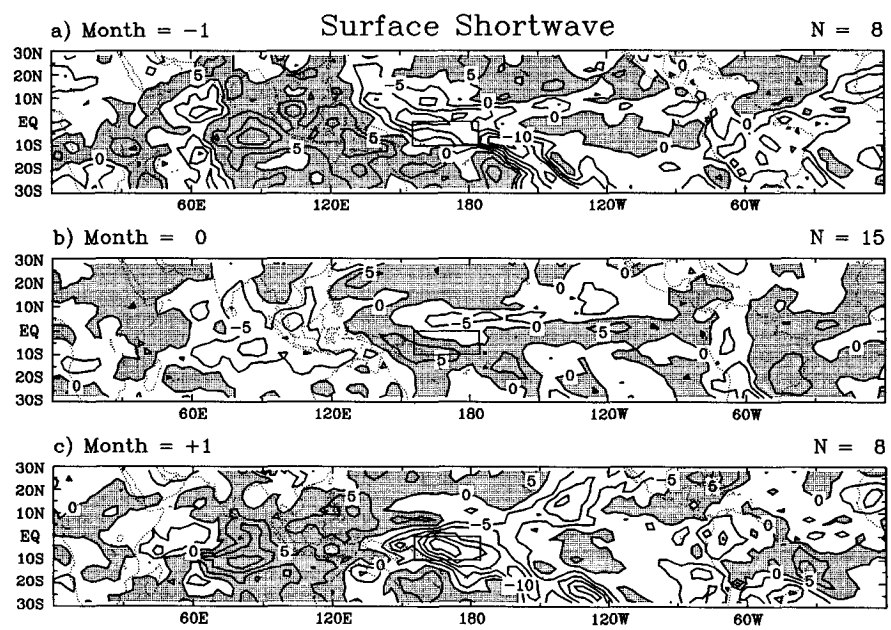

FIG. 10. Same as Fig. 5 except for downwelling surface shortwave radiation; contour intervals are 5 W m^{-2}.

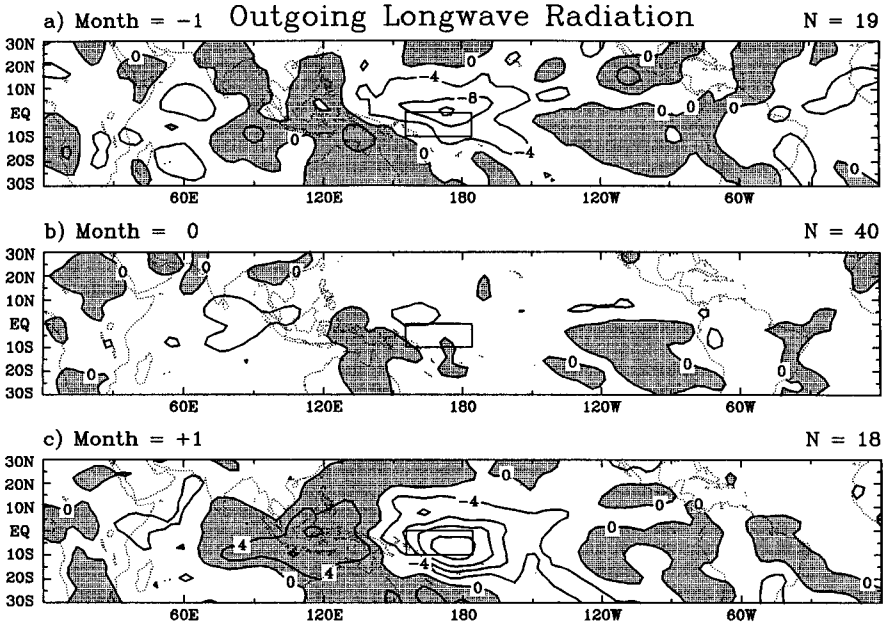

FIG. 11. Same as Fig. 5 except for outgoing longwave radiation; contour intervals are 5 W m^{-2}.

consistent with the maps for top-of-the-atmosphere shortwave cloud forcing from ERBE (not shown).

The results in Figs. 5, 6, 9, and 10, indicate that the SW flux undergoes significantly greater monthly averaged changes during the evolution of ocean hot spots than the surface latent heat flux. In fact, the data analyzed here suggest that the perturbations in SW, induced by the changing convective conditions, are at least a factor of 2 larger than the perturbations in evaporation. Given the manner in which the composite hot spot evolution is presented, the question arises, is the SST cooling observed between the month = 0 and the month = +1 composites attributable to these convection-induced flux changes? The formal approach to this question would entail applying a difference scheme to the SST composites and comparing this to the average "fluxes" across this time period. However, in this case, such a procedure would lead to misleading results since the average anomalies of the dominant surface heat fluxes (SW + latent) across the month = −1,0 composites are roughly the same as that across the month = 0, +1 composites, yet the SST increased over the first time period and decreased over the second. Given that the standard deviation of daily averaged SST in this region is similar in magnitude to the "monthly" changes being discussed here (Weller and Anderson 1995), the production and maintenance of the sustained high SST in the month = 0 composite is very likely the result of the prolonged reduction in convection during this period and possibly the influence of the enhanced fresh water flux occurring in the month = −1 period. Likewise, the decay of this warm SST and the maintenance of the relatively cool SST during the month = +1 composite must be, at least in part, due to the prolonged and/or intense convective conditions occurring during this period.

The evolution of the OLR is shown in Fig. 11. In the warm Tropics, anomalies in OLR mainly reflect variations in high clouds. Therefore, there should be a high degree of consistency with the HRC composites shown in Fig. 6. The main difference between the two figures is that variations in OLR are smoother and have larger spatial scales. The evolution of the cloud field as diagnosed from ISCCP helps elucidate the cloud types responsible for these broad scales as well as those responsible for the changes to the SW discussed above. The evolution of the deep convective clouds (not shown) is very similar to that for the HRC (shown in Fig. 6), with the most apparent difference being an indication of an enhanced (diminished) northern (southern) ITCZ branch similar to the month = 0 SW map (Fig. 10b). Presumably this feature is not as apparent in the HRC composites due to the longer time series for HRC, which averages over more hot spot occurrences (N = 24, 46, 23 for HRC; N = 10, 18, 19 for ISCCP). This suggests that this north–south "dipole" feature in and to the north of the selection region of the SW composites may not be ubiquitous to the formation of all hot spots. In fact, the composites discussed in section 4f indicate this feature stems from particular hot spots associated with the 1986–87 El Niño. Deep convective cloud anomalies in the month = +1 composites over the selection region range up to +8%; a region where the typical climatological values range between about 3% and 19%. Another slight difference is the occurrence of a negative anomaly in deep

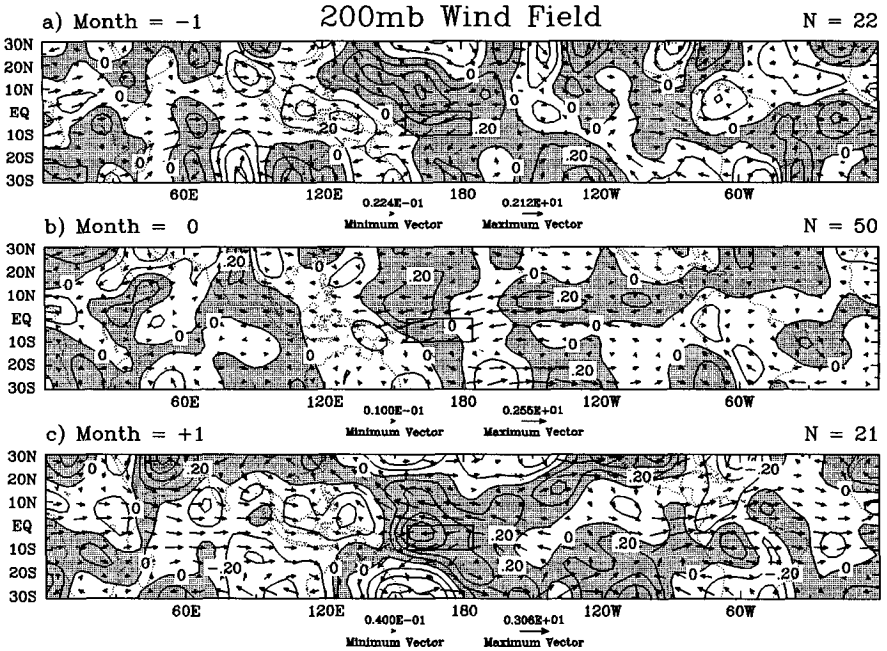

FIG. 12. Same as Fig. 5 except for 200-mb wind field. Contours are horizontal divergence anomalies; contour intervals are 0.2×10^{-6} s^{-1}. Vectors are horizontal wind anomalies (in m s^{-1}). The vector scaling is given at the bottom of each composite. The vectors show the minimum and maximum vectors occurring in each of the individual composites; however, the vector scaling is the same for all three composites.

convection over equatorial Africa in the ISCCP product versus the slight positive one in the HRC. The evolution of cirrostratus clouds, which are defined as having cloud-top pressures less than 440 mb and an optical thickness between about 7 and 23, are very similar to the evolution of deep convection clouds, with nearly the same magnitudes but slightly larger spatial scales of variation. ISCCP cirrus clouds are defined as having cloud-top pressures less than 440 mb and optical thickness less than about 7. As expected, the cirrus cloud anomalies have even broader spatial scales with the largest positive anomalies collocated, or nearly so, with regions of positive anomalous convection, such as over the selection region in the month prior to, and after, the occurrence of the hot spots. This region of anomalous cirrus cloud extends to the west and northwest of the selection region in the month = +1 composite, nearly to 120°E. Figure 6, as well as the ISCCP deep convection (not shown), each show that deep convection is anomalously low over this region. Therefore, it is likely that these cirrus clouds are generated to the east and transported westward by the upper-level flow.

d. Atmospheric circulation

Figure 12 shows the composite 200-mb vector wind field overlaid on the 200-mb horizontal wind convergence. Indeed, the anomalous upper-level flow is westward over much of the selection region and beyond during all three phases. This would account for the westward cirrus outflow from the positive anomalies in deep convection observed in the selection region during the months prior to, and after, the occurrence of the hot spot. As expected, Figs. 12a and 12c also show strong upper-level divergence anomalies coincident with the deep convective cirrus outflow anomalies near the selection region. Each of these composites also indicate enhanced upper-level convergence anomalies to the west, directly over the maritime continent, that correspond, particularly in the month = +1 composite, to weakened deep convection. These two phases (month = ±1) each show anomalous upper-level westerlies from the Atlantic to the central Indian Oceans. This is likely a consequence of the positive (negative) deep convective anomalies over Africa and South America (eastern Indian Ocean). During the month(s) the hot spot occurs, most of the upper-level anomalous structure disappears, except for the formation of anomalous easterlies extending from the western to the central Pacific. This weakening of the Walker circulation is consistent with anomalous suppression of convection in the selection region shown in Fig. 6b and of the large-scale warm ENSO-like conditions that are present.

Figure 13 shows the 850-mb wind field. As expected, most features are anticorrelated with those at 200 mb.

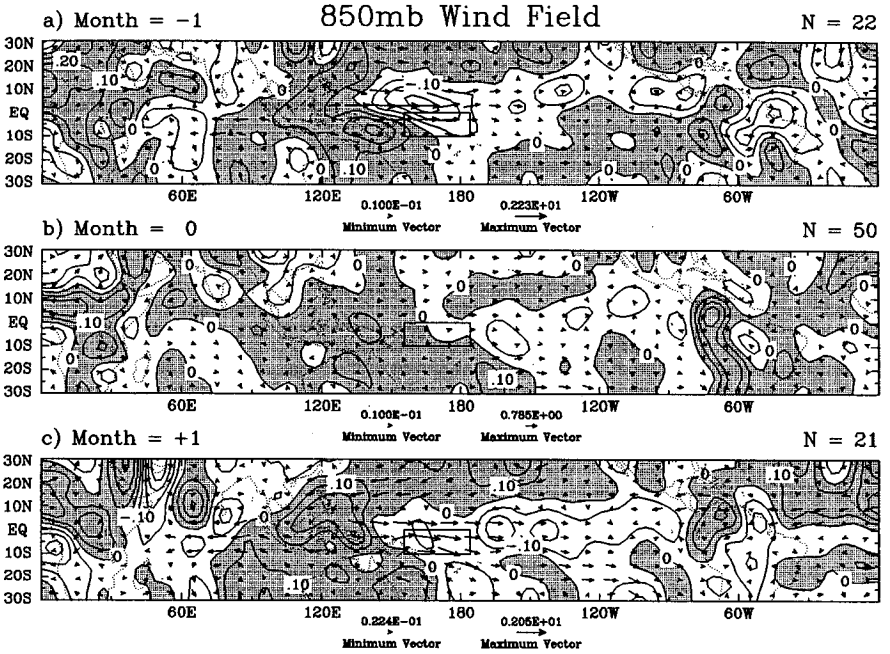

FIG. 13. Same as Fig. 12 except for 850-mb wind field.

During the months before and after the hot spot occurrence, when positive anomalies in convection are present in and near the selection region, there are convergence anomalies coincident with these same regions. These correspond more closely to the convection centers than do the divergence anomalies aloft, which are displaced westward. The low-level winds in these months show anomalous westerlies, consistent with westerly wind burst conditions and the increased surface wind speed observed over the western portion of the selection region shown in Figs. 7a and 7c. Figure A1d shows the degree these composite to composite changes averaged over the selection region are statistically significant. As with the 200-mb wind pattern, the 850-mb month = 0 map shows almost no anomalous pattern. Note that while the deep convection anomaly, as represented by the HRC, is much stronger in the month = +1 than the month = −1 composite, the 850-mb convergence anomaly is weaker in the month = +1 composite.

Figure 14 shows longitude–height circulation composites averaged between 2°N and 12°S. The vertical and horizontal vectors show anomalous vertical and zonal velocity, respectively, and the contours show anomalous horizontal convergence. The two vertical lines show the longitude boundaries of the selection region. Consistent with previous figures, Fig. 14 shows strong vertical velocity anomalies ($\sim$10 mb day^{-1}) in the month = ±1 composites associated with the enhanced deep convection. Enhanced vertical motion is also seen in these same composites over the South American continent and to some degree over Africa and the west Indian Ocean. Enhanced subsidence associated with large regions of anomalous upper-level convergence is observed in the month = ±1 composites over the maritime continent. In the month = 0 composite, the conditions are fairly benign, with modest upper-level convergence and subsidence on the eastern edge and to the west of the selection region. These regions of enhanced subsidence presumably contribute to the diminished convection observed in the selection region during the occurrence of the hot spot. During this period, there are also modest westward anomalies in the upper-level flow across most of the Pacific basin. The month = +1 composite also shows that the maximum convergence anomaly over the selection region is displaced upward to the 500–700-mb layer and, as mentioned above, is not as evident at the 850-mb layer.

The corresponding pressure–longitude composite of temperature anomaly (not shown) indicates many similarities between the three phases. In general, each has positive upper-level ($p < 600$ mb) temperature anomalies, positive low-level temperature anomalies over most of the Pacific basin, and negative low-level anomalies from South America eastward to about 160°E with particularly strong negative anomalies ($\sim$1.2°C) over Africa and South America. The upper-level anomaly strength ranges from about 0.0°–0.3°C, 0.0°–0.1°C, and 0.1°–0.5°C for the month = −1,0,+1 composites, respectively, with the strongest anomalies occurring over Africa and the Pacific Ocean, particularly in the month = +1 composite. Over the eastern portion of the selection region, the low-level anomalies are about −0.3°C with the negative anomaly extending farthest

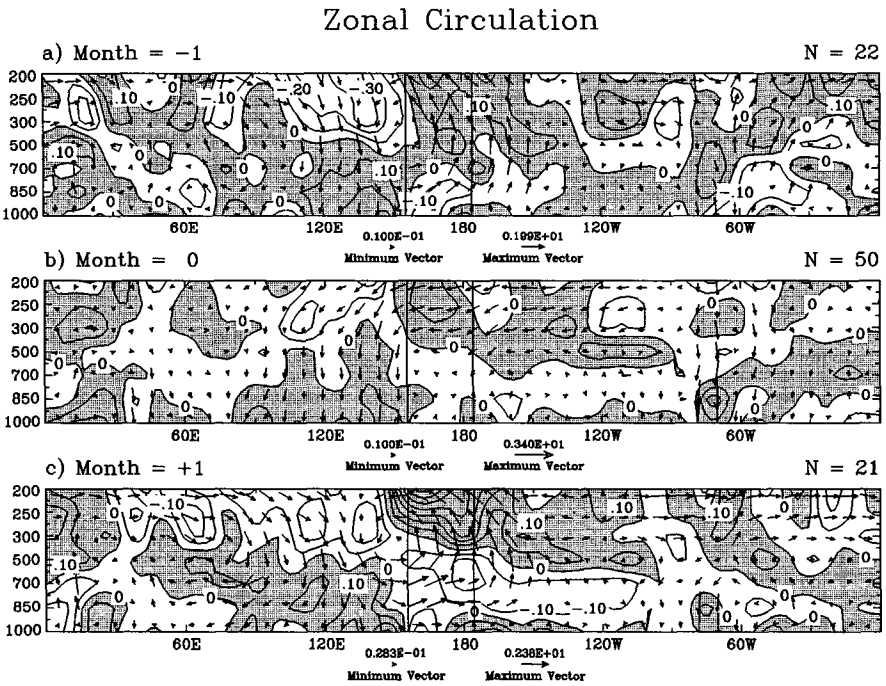

FIG. 14. Same as Fig. 5 except for composite zonal circulation anomalies as a function of pressure and longitude. Latitude averages were computed between 2°N and 12°S. Contours are horizontal divergence anomalies; contour intervals are 0.1×10^{-6} s^{-1}. Horizontal vectors are zonal wind anomalies in m s^{-1}, and vertical vectors are vertical velocity anomalies in mb s^{-1}. The vector scale is given at the bottom of the figure; vertical velocities were multiplied by 2×10^4. The scaling vectors show the minimum and maximum vectors occurring in each of the individual composites; however, the vector scaling is the same for all three composites. Vertical lines denote the longitude extent of selection region.

east (180°) and upward (~600 mb) during the month = +1 composite. During the month = 0 composite, the temperature anomaly is fairly homogeneous from 700 mb and up, with a slight warming (~0.1°C) occurring over the Pacific basin.

Figure 15 shows the relative humidity pressure–longitude composites, which show considerable changes during the course of the three phases. Most noticeable is the development of a weak large-scale dry anomaly during the month = 0 composite from the surface to midlevels over most of the selection region and to the east. This region of drying corresponds to the slight subsidence observed in the zonal circulation composite of Fig. 14b, and likely contributes to the depressed convective conditions observed during the month = 0 composite. Intense drying (−1% to −6%) is also observed in the regions over the maritime continent exhibiting anomalous subsidence, especially in the month = ±1 composites. The reduced drying observed in this same region in the month = 0 composite is likely due to the modest enhancement of convection in this region during this phase of the evolution. In the months before and after the occurrence of the hot spot, positive mid- and upper-level anomalies in relative humidity, up to 8% in the month = +1 composite, develop in and near the selection region. As indicated above, this moistening is associated with positive anomalies in deep convection and is coupled with positive temperature anomalies, and therefore indicates more absolute water vapor.

Composites of the anomalous meridional circulation (not shown) averaged between 156°E and 176°W are consistent with the previous view showing strong upper-level divergence anomalies (peak values ~0.5 $\times 10^{-6}$ s^{-1}), particularly in the month = ±1 composites, coupled with low-level convergence (~0.2 $\times 10^{-6}$ s^{-1}). Again, the low-level convergence anomaly is shifted up from about 850 mb in the month = −1 composite to about 600 mb in the month = +1 composite. Associated with this enhanced convergence at 600 mb are positive convergence anomalies (~0.2 $\times 10^{-6}$ s^{-1}) at the 1000-mb level, at about 10°N and 15°S, with weak divergence in between. Each of the composites show an enhancement of the southern branch of a two-celled Hadley-type structure, with a strong development of the northerly branch occurring over the course of the three phases.

The corresponding pressure–latitude composites of temperature are shown in Fig. 16. The temperature anomaly patterns each show anomalous warming

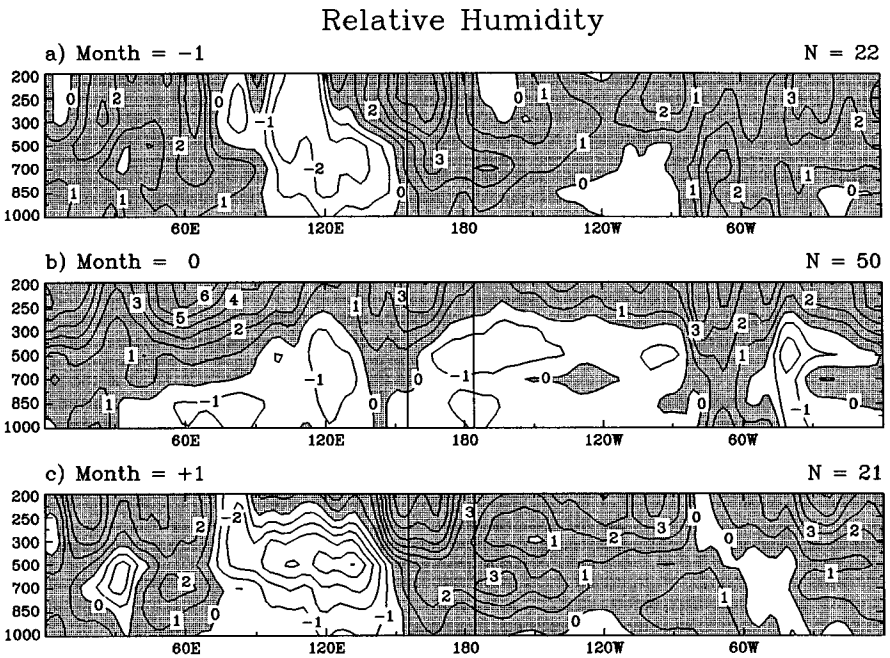

FIG. 15. Same as Fig. 14 except for composite relative humidity anomalies; contour intervals are 1%.

throughout the domain except near the surface poleward of 10°. This is consistent with the overall mean tropical SST warming observed in Fig. 5 and the tendency for enhanced deep convection in and near the selection region, particularly before and after the occurrence of the hot spot. The month = 0 positive anomalies are on the order of 0.1°–0.2°C, while those of the month = ±1 composites range from 0.2° up to 0.6°C. The temperature anomaly in the near-equatorial, near-surface region disappears in the month = +1 composite. This could be due to the transport of cooler air from the subtropics or from the region to the west, each of which exhibit negative temperature anomalies. It could be also be due to enhanced vertical exchange from the increase deep convection. In any case, Fig. 16c indicates that a fraction of the heat removed from the surface layers of the ocean goes into heating the upper troposphere by up to 0.5°C. The associated pressure–latitude composites of relative humidity (not shown) indicate many of the same features discussed above (Fig. 15). During the month = ±1 composites, there are positive relative humidity anomalies between 20°S and 15°N at the surface extending up to 15°S and 20°N at 200 mb. The anomalies range from about 1% at 900 mb and increase approximately linearly upward to about 5% at 200 mb. There are areas of drying outside of this region extending from the surface to 200 mb, which are generally consistent with the regions of anomalous subsidence shown in meridional circulation composite (not shown). During the month = 0 composite, the pattern changes considerably to one with low-level drying throughout the lower troposphere, of about 1%, with a particularly pronounced negative anomaly extending from the surface to 400 mb and from the equator to about 10°S, with a −2% maximum at about 850 mb and a −3% maximum at about 500 mb. The statistical significance of the changes that occur at 500 mb is illustrated in Fig. A1e. The degree of upper-level moistening in the month = 0 composite is generally between +2% in the Southern Hemisphere and +3% in the Northern Hemisphere at about 300 mb and above.

As discussed near the beginning of this section, the global-scale organization of the deep convection pattern, along with the typical timescale of formation and decay of the ocean hot spots, suggests a possible link to the 30–60 day oscillation. Reexamination of the HRC composites show that the month = ±1 composites have a wavenumber 2 modulation to them with convection enhanced near the selection region as well as over the longitudes near Africa and South America. The month = 0 composite has a weak dipole feature in convection with suppressed convection over the selection region and enhanced convection over the eastern Indian Ocean, in addition to enhanced convection over South America. These HRC anomaly patterns along with the associated 250- and 850-mb wind patterns show some similarity to certain phases of the composite Madden–Julian oscillation (MJO) constructed by Hendon and Salby (1994, hereafter HS) using daily data filtered to select timescales of 35–90 days and wavenumbers 1–3. Most similar are the month = +1 com-

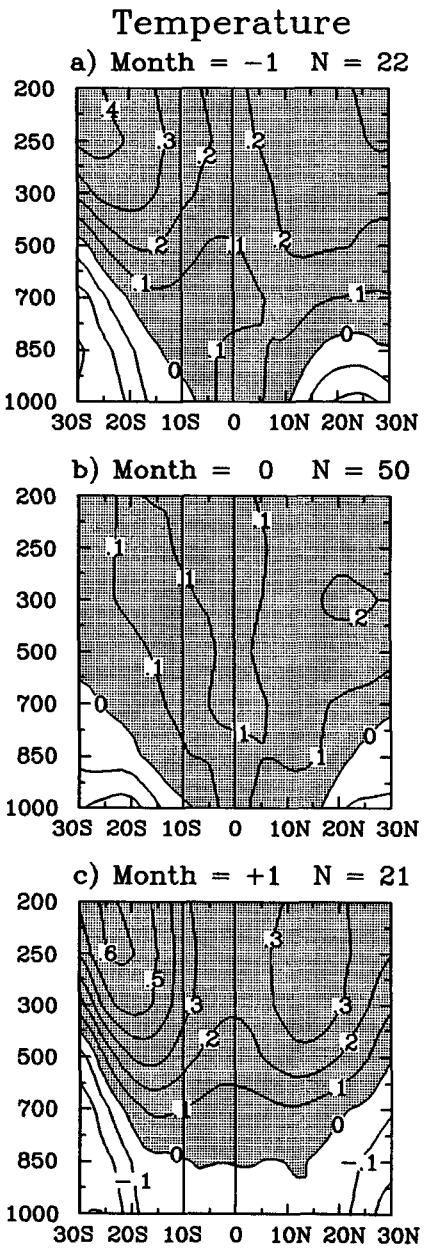

FIG. 16. Same as Fig. 5 except for composite temperature anomalies as a function of pressure and latitude; contour intervals are 0.1°C. Longitude averages were computed between 156°E and 176°W.

posites presented here and the "lag = 25 day" composites of HS (shifted eastward by about 20°). In this phase of the MJO, the principal convection center has already propagated from the African continent across the Indian Ocean to the western Pacific. That the lifetime of these ocean hot spots is one month would suggest that by traversing back 30 days in the HS composites, that is, to "lag = −5 days," is analogous to the month = 0 composite presented here. With respect to the convection field, this is partially true in that it tends to be enhanced in the Indian Ocean and suppressed in the western Pacific with some upper-level convergence near the date line. However, most other aspects of the composites do not match that well. The month = −1 composites have some resemblance to the HS "lag = −15 day" composite, when the MJO has a strong wavenumber 2 pattern, as well as to their "lag = 25 day" composite.

These results indicate a possible link between the MJO and the formation/decay of the ocean hot spots. First, the spatial organization induced by the MJO leads to regions of anomalous subsidence, which are favored regions for hot spot formation. Second, the eastward motion of the MJO eventually carries a zone of anomalous low-level convergence and positive vertical motion into the high SST region to initiate/enhance the decay of the ocean hot spot. The remarkable similarity of the month = +1 composites presented here and in the later phases of the HS composites indicates that many hot spots do tend to dissipate in association with MJO phases that place enhanced deep convection over the western Pacific. While there is reduced similarity between the month = 0 composites and the earlier MJO phases identified by HS, this study's data were not filtered to select only intraseasonal variability, as was done in HS, and the associated MJO variability is likely being masked by episodes of strong interannual variability. Furthermore, the selection criteria and compositing methods used here allow for several sequential months to be composited together (e.g., Fig. 4c), which could average together more than one phase of an MJO. This latter point emphasizes that the MJO, and its associated timescale, is not the only important process involved, and that longer timescales and possibly ocean processes are probably important as well.

e. Composite ocean

The previous section described the evolution of the atmospheric conditions associated with the development and decay of very warm SST in the western Pacific Ocean. This section uses the results from the NMC ocean analysis system to examine the evolution of the three-dimensional structure of the ocean. Figure 17 shows the surface wind stress fields used to force the model and the resulting anomalous sea level. The contours represent sea level and the vectors represent surface wind stress. The large-scale patterns of surface stress, sea level, and divergence (not shown), which are similar in each phase, are consistent with the modest El Niño phase observed in the SST composites (Fig. 5). There are negative (positive) anomalies in sea level in the western (central and eastern) Pacific, strong westerly wind stress anomalies along the equator between about 140°E and 150°W, and a strong surface convergence anomaly (not shown) along the equator in nearly this same longitude range. During the month

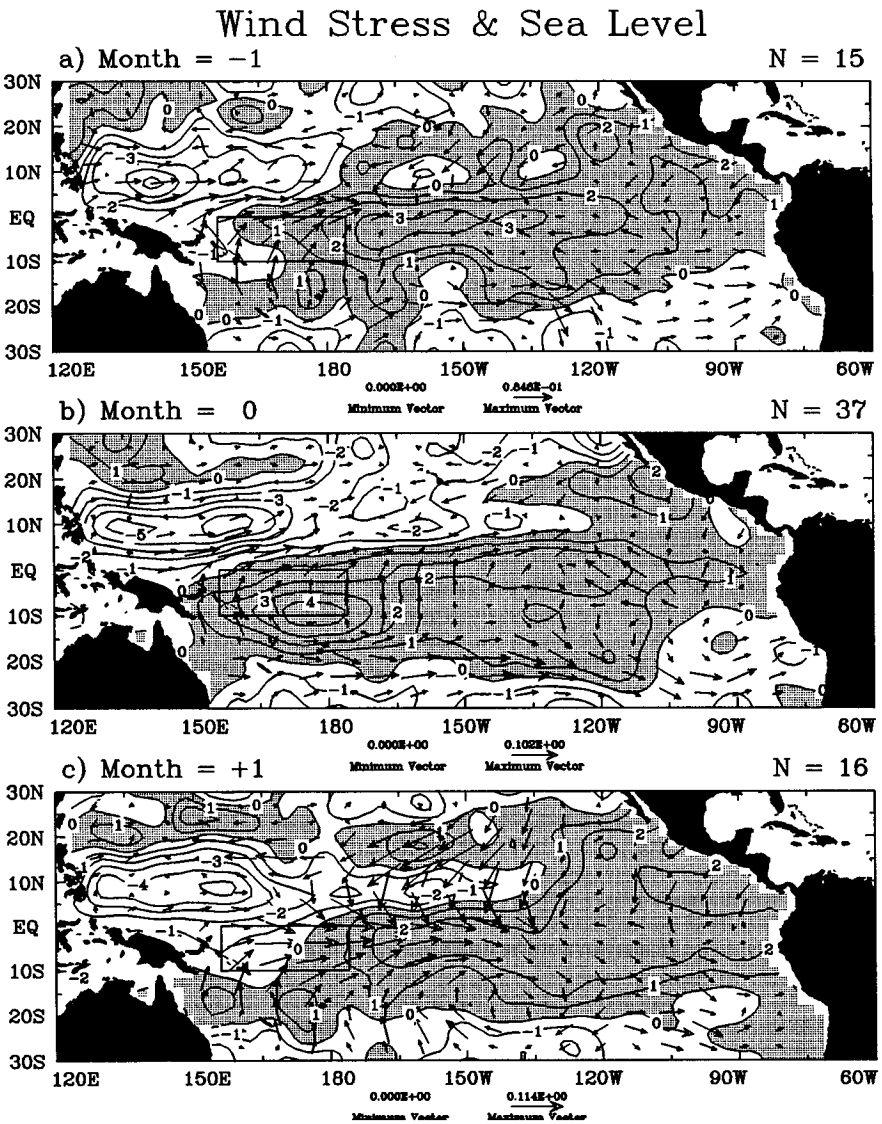

FIG. 17. Same as Fig. 5 except for ocean-surface wind stress and sea level. Contours are sea level anomalies; contour intervals are 1 cm. Vectors are horizontal wind stress anomalies in dynes cm^{-2}, with the scale given at the bottom of the figure. The scaling vectors show the minimum and maximum vectors occurring in each of the individual composites; however, the vector scaling is the same for all three composites.

= 0 composite, there is a positive sea level anomaly nearly coincident with the selection region, and thus the maximum SST anomaly. The temperature anomaly composites discussed below suggest this sea level anomaly can be attributed mostly to steric height anomalies. The month = 0 composite also tends to have the weakest westerly wind stress and equatorial convergence anomalies (not shown) out of the three phases.

Figure 18 shows the composite meridional cross sections of ocean temperature anomaly, averaged across the selection region. These indicate a near-surface temperature (5 m) evolution similar to that shown by the SST in Fig. 5. However, the figure also indicates that during the course of the (surface) hot spot evolution, the selection region undergoes temperature anomaly fluctuations that extend down beyond 200 m in depth. These fluctuations are confined generally southward of about 5°N, where a warm anomaly in the month = −1 composite extends from the surface to about 100 m, grows in magnitude and depth in the month = 0 composite, and then nearly disappears in the month = +1 composite. Throughout this evolution, there is a stationary cold anomaly at about 8°N extending from about 70–200 m with a magnitude as large as −0.8°C.

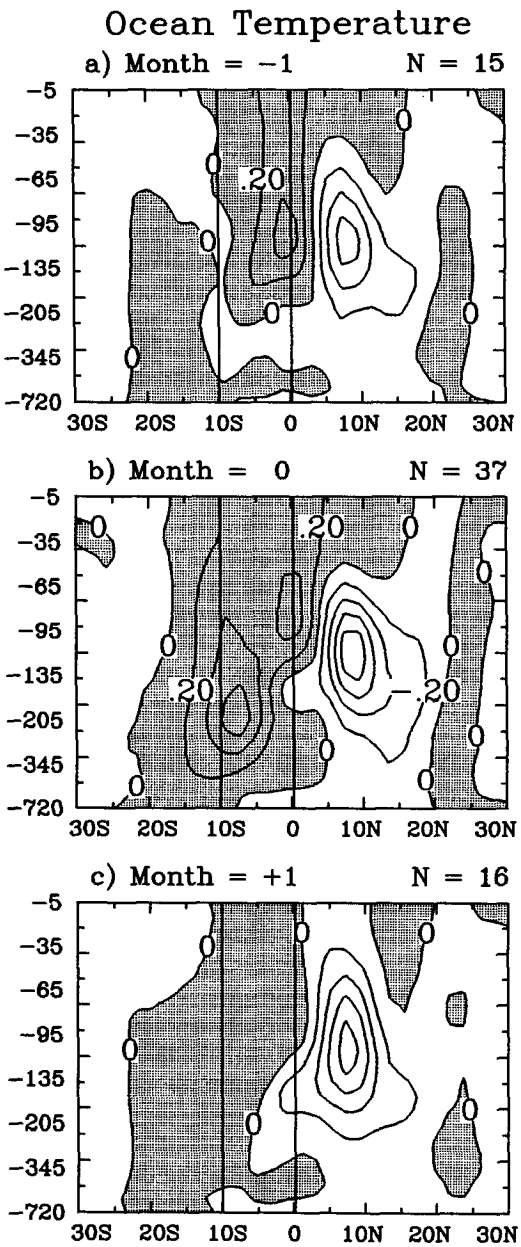

FIG. 18. Same as Fig. 5 except for depth–latitude composites of ocean temperature anomalies; contours intervals are 0.2°C. Longitude averages were computed between 156°E and 176°W. Note the depth coordinate scale matches the model vertical grid and therefore appears stretched. Vertical lines denote the latitude extent of selection region.

Estimates of the heat content for the selection region down to 720 m provide an estimate of the heat flux anomalies that are required to induce the indicated temperature changes. Assuming that changes between the month = 0 and month = +1 composites occur over the time period of one month suggests that the required heat flux is on the order of −190 W m^{-2} for the selection region. These results, and those earlier pertaining to the surface heat budget, suggest that ocean heat transport and/or ocean mixing are playing a nonnegligible role in the evolution of the upper-layer surface heat budget in these regions during these time periods. In fact, the perturbations to the surface shortwave and evaporation discussed earlier are really only consistent with the changes in temperature occurring over about the upper 80 m. In the next section it is shown that this heat balance is strongly modified by the presence of El Niño–type conditions in these composites.

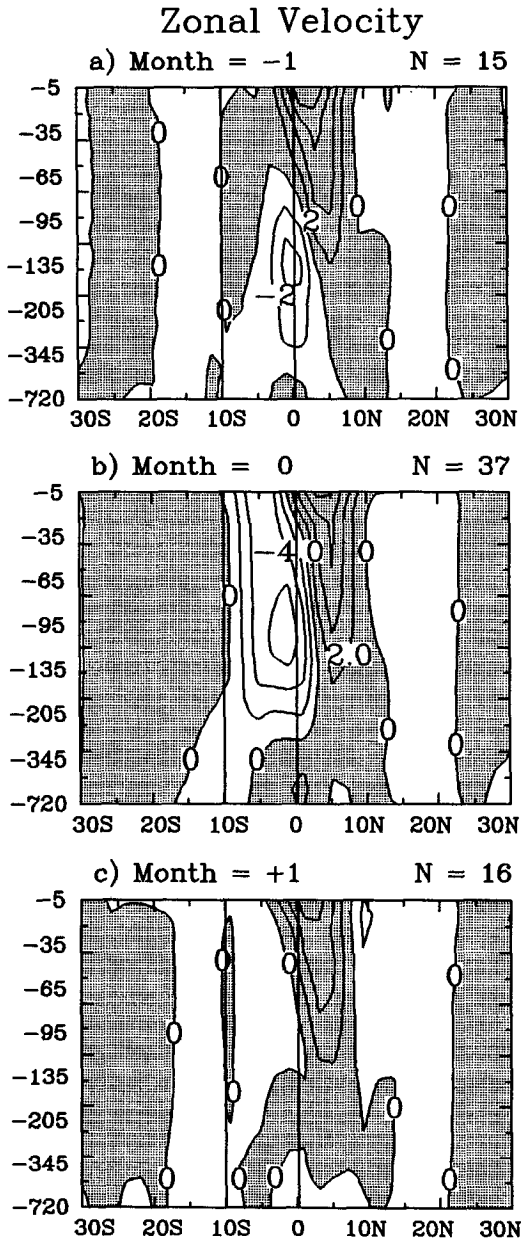

FIG. 19. Same as Fig. 18 except for zonal velocity; contour intervals are 2 cm s^{-1}.

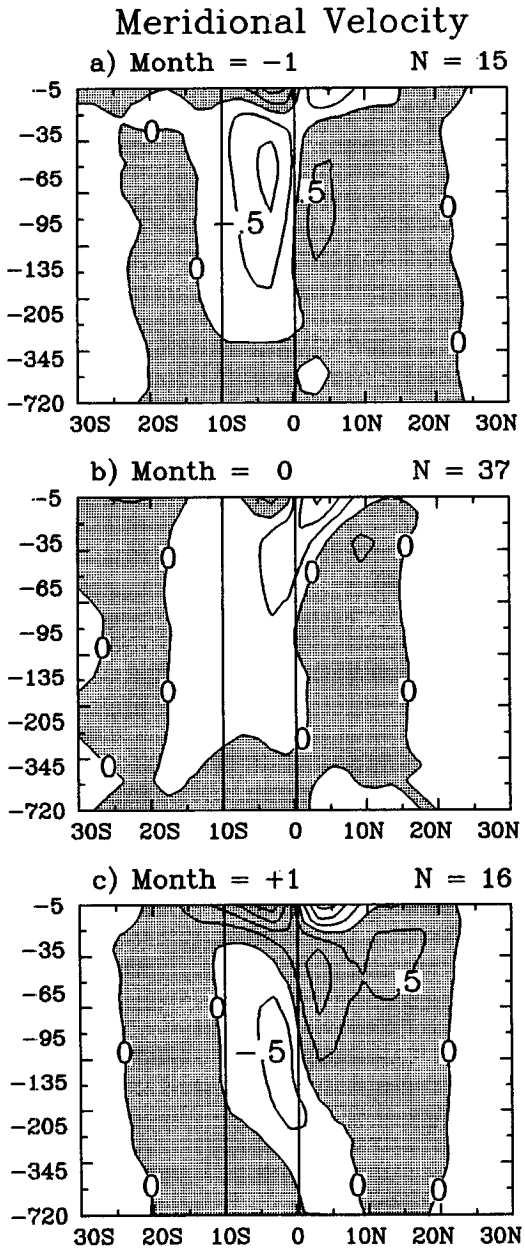

FIG. 20. Same as Fig. 18 except for meridional velocity; contour intervals are 0.5 cm s^{-1}.

Figures 19 and 20 show depth–latitude composites of anomalous zonal and meridional velocity, respectively. Among all three composites there is anomalous convergent meridional velocity near the surface at the equator and divergent velocity at about 80 m (each about 1–2 cm s^{-1}). However, the strength of these anomalous meridional circulation cells is significantly reduced during the month = 0 composite and then enhanced again during the month = +1 composites, presumably due to the evolving near-equatorial wind stress and sea level patterns discussed above. Figure 19 shows positive zonal velocity anomalies, of about 2–8 cm s^{-1} extending from the surface at the equator down to about 100 m at 5°N. Developing during the month(s) the hot spot occurs is an easterly zonal current anomaly of about 6 cm s^{-1} at about 100 m, extending from the equator to about 6°S. The statistical significance of the changes in zonal velocity anomaly that occur at 60 m is illustrated in Fig. A1e. Composite meridional cross sections of anomalous horizontal convergence (not shown) indicate that the largest contributions are made by the meridional velocity (i.e., dv/dy) and that the largest anomalies are contained in the upper 20 m. However, there are weaker divergence anomalies at depth in the month = ±1 composites on the equator with magnitudes of about $0.5–1.0 \times 10^{-8}$ s^{-1}. These extend from about 25 m down to 100 m. A secondary divergence maximum occurs at about 300 m in the month = +1 composite, which is more directly related to contributions from the zonal velocity.

While the NMC ocean assimilation product described above does not include sufficient information to address the absolute impact of the near-surface, internal ocean heat flux changes,[4] it does illustrate that the ocean, as well as the atmosphere, is evolving rapidly during the formation and decay of these ocean hot spots. This suggests that the ocean component is far from an inert, surface mixed layer of constant depth that is often invoked in many studies addressing limiting mechanisms on SST. In fact, the next section illustrates that with respect to the formation and decay of hot spots, the ocean is significantly more sensitive

[4] Only monthly mean quantities are provided with no information on eddy transports. Moreover, since the model is run in assimilation mode, there are artificial heat sources/sinks that are not represented by the elementary terms.

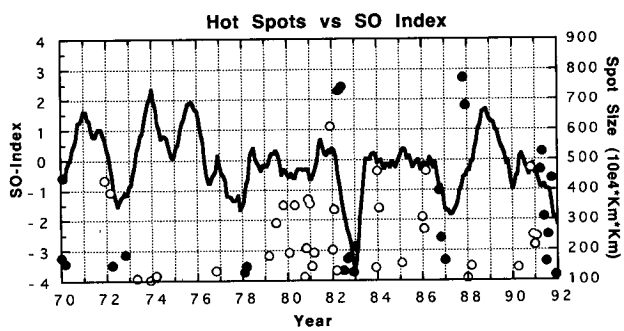

FIG. 21. Time series of Southern Oscillation index (SOI; solid line) along with scatter diagram showing the sizes and months of occurrence of the hot spots from the western Pacific warm-pool selection region. These points (filled and open) are the same points as the filled diamonds in Fig. 2. In this plot, the filled circles indicate hot spots occurring during low SOI phases (e.g., El Niño) phases. The SOI was smoothed using a 5-month box-car filter.

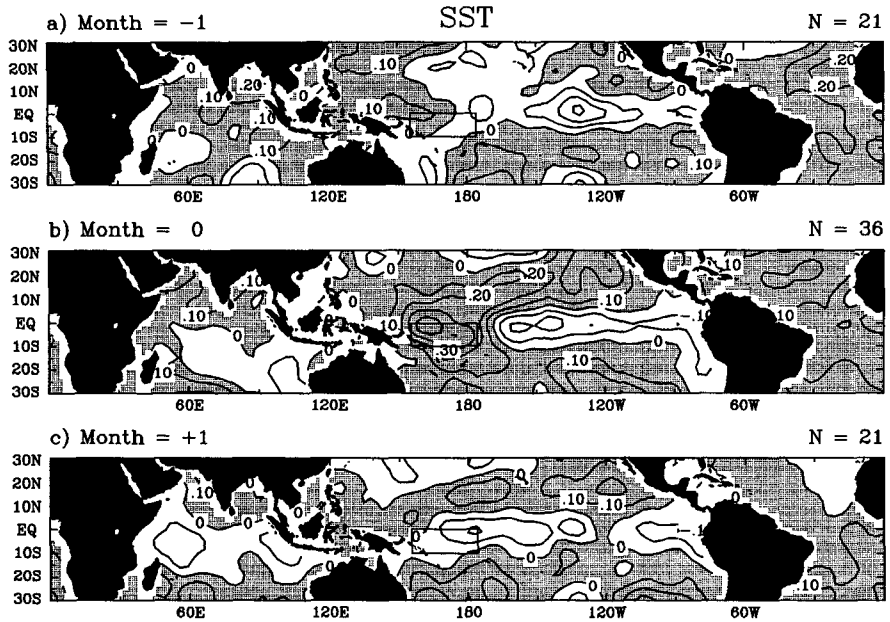

FIG. 22. Same as Fig. 5 except the composites do not include the hot spots indicated by the filled circles in Fig. 21.

than the atmosphere to the interannual state of the system.

f. ENSO influence

The discussion of temporal variability of hot spot formation in the western Pacific in section 4a, along with the atmosphere and ocean composites discussed above, indicates that ENSO dynamics and thermodynamics may play some role in the frequency of very warm water formation and possibly in the manner it decays. Specifically, the overall composite, mean-anomalous structures, particularly that of SST, look similar to climate anomalies associated with a weak but warm ENSO phase. Figure 21 shows a smoothed time series of the Southern Oscillation index (SOI) for the analysis period. Replotted on this graph, as a scatter diagram, are the months of occurrence and sizes of the hot spots that occurred in the selection region, that is, all the same points that were plotted as filled markers in Fig. 4b. In this case, however, the filled markers are hot spots forming in the selection region during a warm ENSO time period and thus are those hot spots that are most likely contributing to the large-scale, weak El Niño pattern observed for example in Fig. 5. The selection criteria for these points is any hot spot that formed during a month when the SOI fell below −0.5 during a sustained ENSO event in which the index at some point dropped below −1.0. Evident from this figure is the fact that many of the hot spots form during time periods that are not associated with an El Niño period, but few form during time periods that are associated with a La Niña period. This section describes the composite patterns when these "El Niño" hot spots are removed from the averaging procedure, hereafter ENR composites, to illustrate what aspects are modified from the composites described above with all the hot spots included, hereafter AHS composites.

Figures 22 and 23 are analogous to Figs. 5 and 6, respectively, but for the composites in which the low SOI hot spots have been removed from the averages. Analogous to Fig. A1a, Fig. A1f shows the statistical significance of the corresponding changes that occur in SST and HRC averaged over the selection region. As expected, the overall SST anomaly pattern is now biased more toward a weak La Niña condition with cold anomalies along the equator, particularly in the central and eastern Pacific. The SST anomaly in the selection region is slightly cooler in all three composites than for the AHS case, not getting quite as warm in the month = 0 composite and cooling slightly more in the month = +1 composite. The HRC patterns for the ENR composites still show evidence of the same large-scale organization. While the positive anomaly in HRC in the month = −1 composite has been shifted west by about 30°, evidence from other fields suggest that there is still enhanced vertical motion over much of the selection region with divergence occurring at midlevels rather than upper levels (e.g., enhanced midlevel rather than high clouds). The month = 0 composite retains the qualitative pattern of anomalously high convection over the eastern Indian Ocean and suppressed convection over the selection region. In this case, however, each of the anomalies is enhanced over the AHS case.

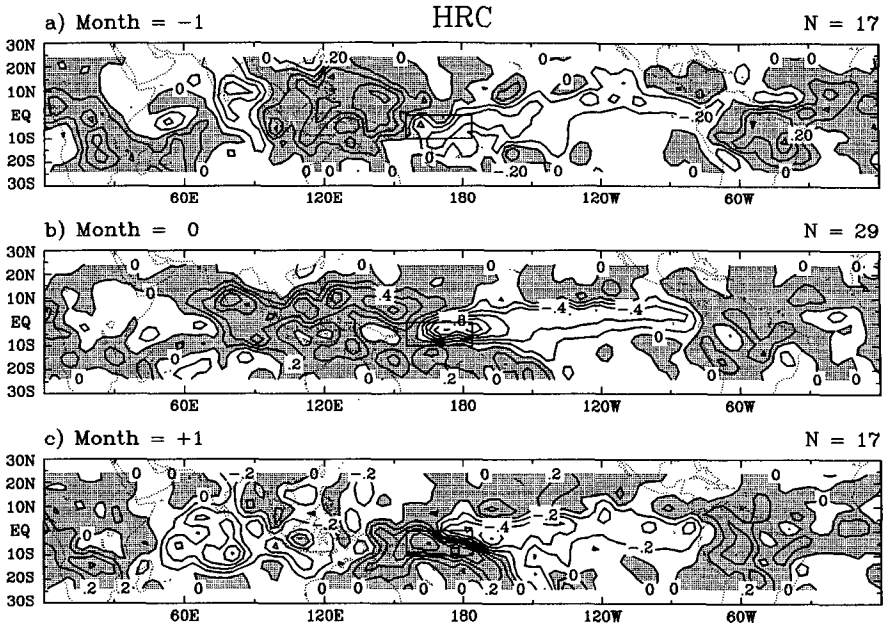

FIG. 23. Same as Fig. 6 except the composites do not include the hot spots indicated by the filled circles in Fig. 21.

The month = +1 composite is the most similar of the three composites to the AHS case, with the main difference that the dipole pattern in convection between the anomalously low values over the Indian Ocean and the high values over the selection region is shifted slightly westward. Finally, in all three composites, much of the equatorial Pacific basin east of the selection region exhibits anomalously low convection.

In the interest of space, plots of the other ENR composites will not be shown but will be discussed briefly to highlight their main differences from the AHS composites. With regard to the surface fluxes, the negative wind speed anomalies tend to be stronger and envelope more of the selection region area. This leads to reduced $(Qs - Qa)W$ anomalies in the month = +1 composite (cf. Fig. 9); less (more) area of positive (negative) anomalies near the western (eastern) half of the selection region. The ENR composites show a relative increase in the area and magnitude of the positive shortwave anomalies over the selection region in the month = 0 composite, with values over 10 W m^{-2}. This composite also reveals that the removal of the El Niño hot spots results in the removal of the north–south dipole anomaly associated with the ITCZ in, and to the north of, the selection region of Fig. 10b and indicates that this feature was mostly the result of specific hot spots that occurred in association with the 1986–87 El Niño. The month = +1 SW composite is very similar to the AHS case over most regions, with the reductions in SW during this period of about 20 W m^{-2}.

Inspection of the dynamic fields, such as the zonal and meridional circulation composites (cf. Figs. 14) along with the 200- and 850-mb wind fields (cf. Figs. 12 and 13), indicates that the spatial locations of the upper- and lower-level divergence patterns are largely the same, with the primary exception being that peak anomalies in and near the selection region are displaced slightly westward. Further, the strength of most of the anomalies has increased, particularly in the case of the subsidence region near the eastern portion of the selection region during the month = 0 composite. Pressure–longitude composites of temperature anomalies generally indicate a relative cooling at lower levels, particularly over the Pacific basin, while the relative humidity composites indicate significant drying relative to the AHS composites over most of the mid-to-upper troposphere. This drying extends down to the surface over most of the Pacific, with particularly strong anomalies (up to −4%) near the eastern portion of the selection region.

The composites described above indicate that while removing the El Niño–period hot spots did alter some large-scale aspects of the atmospheric composites, it left the overall temporal and spatial relationships between the variables the same, particularly with respect to the large-scale organization of deep convection (HRC) and the relationship between deep convection and SST in and near the selection region. However, many aspects of the ocean composites changed considerably. Fundamental differences include a shift to generally positive sea level anomalies in the west and negative anomalies in the east, an overall increase in the magnitude of the South Equatorial Current, and a reversal from anomalous surface convergence along the

equator in the AHS case to anomalous divergence. These changes are all associated with the surface zonal wind stress changing from westerly stress anomalies in the AHS cases to enhanced easterly stress in the ENR cases. One difference to note is that while the sea level anomaly in the selection region disappeared in the month = +1 AHS composite, presumably due to the cooling that was observed to occur over depth (Fig. 18), the sea level anomaly in the ENR month = +1 composite remains. The temperature–depth composites show that the warm anomaly is not reduced at depth in the ENR month = +1 composite and that the cooling only reaches to about 50 m. Again, the estimated perturbations to the SW and evaporation are consistent with the heat content anomalies in the upper 100 m or so. Associated with these differences in the large-scale surface fields are corresponding changes in the meridional circulation. For example, the anomalous meridional circulation "cells" evident in Fig. 20 have reversed; however, the relative changes in the near-surface circulation between the composites is similar. The positive zonal velocity anomalies extending from the surface down to about 100 m in each of the composites of Fig. 19 has generally disappeared, although the development of a negative anomaly in the equatorial undercurrent during the month = 0 composite still occurs and even remains during the month = +1 composite.

The differences between the composites with and without the warm ENSO-phase hot spots indicate that the inferences made concerning the nature of the thermodynamic and dynamic links, at least those between the atmosphere and ocean surface, do not change appreciably. Inclusion of warm ENSO periods appears to favor the development of hot spots in the selection region, favor the formation of very large hot spots ($>5 \times 10^6$ km^2) (Fig. 21), modify slightly the relative importance of the shortwave and latent heat flux perturbations, and possibly help to increase the lifetime of the ocean hot spots. This last point is illustrated by Fig. 4c, which in addition to showing the typical lifetimes of the AHS hot spots (filled bars), shows the number of occurrences for the ENR hot spots (gray bars). While the numbers are small in most cases, there is a relative reduction of long-lifetime spots over the hot spots that last one month. Given the apparent instability of large hot spots (e.g., Fig. 2) and the overall climate changes in the atmosphere and Pacific Ocean associated with ENSO, for example, a reduction in upper ocean heat content, this behavior is not unexpected.

5. Summary and discussion

The goal of this study was to examine the manner in which the ocean and atmosphere combine to limit the observed climatological values of SST to values below about 30°C. Within this goal was an effort to first examine the spatial and temporal variability of very warm SST. The results of this analysis showed that large areas ($>10^6$ km^2) of ocean surface with temperatures greater than 29.75°C occur almost exclusively within the 28°C isotherm of the long-term mean SST field. Particularly high concentrations of these ocean "hot spots" occur, as expected, in the warm pool region of the western Pacific. Other regions of high hot spot concentrations are the northern Indian Ocean and, to a lesser degree, the South China Sea, off the northwestern coast of Australia and in the northwestern tropical Pacific Ocean. Analysis of their temporal variability shows that 1) tropical Pacific La Niña conditions appear to inhibit hot spot formation, particularly in the Pacific warm pool, 2) Southern (Northern) Hemisphere summer conditions favor hot spot development in the warm pool (Indian Ocean), and 3) the typical lifetime of an ocean hot spot is about 1 month, with several lasting 2–3 months, and only a couple lasting more than 3 months. This suggests that the formation of this exceptionally warm surface water preferentially occurs when conditions are favorable on interannual, annual, and intraseasonal timescales. Further, the typical size and timescales characterizing ocean hot spots (Figs. 2 and 4c) indicate that large areas of very warm water in the Tropics, even within 0.5°C of climatology, are quickly damped by the coupled ocean–atmosphere system back to "equilibrium."

A compositing analysis was performed in order to try to understand the evolution of the hot spots that form in the western Pacific warm pool. Large-scale, three-dimensional ocean and atmosphere conditions for the months before, during, and after the occurrence of the hot spots were composited in order to develop a four-dimensional picture of the evolution of this very warm SST. The data were taken from a variety of sources including in situ data, satellite-derived products, and ocean and atmosphere model analysis fields in order to reduce the reliance on any particular time period or dataset. The intention was to use these composites to 1) understand what local thermodynamic mechanisms combined to form and then dissipate areas of very high SST, 2) provide a link between these local mechanisms and the large-scale, or remote, dynamical forcing conditions, including the intraseasonal timescale, and 3) begin to examine the role of ocean processes in this phenomena.

The composite analysis for SST and deep convection showed two important features. First, that SST and deep convection tended to be out of phase with respect to the formation and decay of ocean hot spots. The warmest SST occurs during suppressed deep convection and is followed by a cooler SST during enhanced deep convection. This indicates the important role that internal, or remotely forced, atmospheric forcing plays in suppressing deep convection and allowing the formation of the ocean hot spots (e.g., WG). Second, the dynamical composites, such as 200- and 850-mb wind, along with the large-scale organization of the HRC,

suggest that this atmospheric forcing may stem from the Madden–Julian oscillation. This 30–60 day timescale mode of tropical variability tends to produce alternating regions of atmospheric subsidence and deep convection in the near-equatorial regions, typically with a wavenumber 2 modulation. It was found that the ocean hot spots tend to form in the western Pacific when convection is suppressed over this region in favor of enhanced convection to the west, over the Indian Ocean (e.g., Figs. 6, 11, 12, 14, 23). The atmosphere over the hot spot is left anomalously clear with the composites showing anomalous drying at low and midlevels, which further helps to inhibit the formation of convection over the warming hot spot. The formation of the hot spot is further aided by increases in downwelling shortwave radiation at the surface relative to the before and after composites, and by slightly decreased wind speeds, which in turn would seem to reduce the surface latent heat flux. However, similar to the findings of WG, concomitant increases to $Qs - Qa$ appear to offset, and even outweigh, this latter effect. It is interesting to consider whether the impact of the enhanced precipitation occurring during the month $= -1$ composite over the selection region ($\sim$60 mm mo^{-1}) perturbs the mixed-layer depth enough to predispose the ocean surface layer to an enhanced warming.

The cool periods preceding and following the hot spot are associated with strong enhancements to convection that appear to occur when a vertical ascent region coincides with the hot spot. This condition appears to be brought on by an MJO moving across the warm pool area (cf. Figs. 6, 12, 13, 14, and HS); however, the data do not exclude the possibility that in some cases the SST warming itself may be enough to organize the enhancements to the large-scale convection. Commensurate with the positive convective anomalies are perturbations to the surface energy fluxes. The two dominant components of the surface heat budget in the warm tropical ocean regions are the fluxes of latent heat and shortwave radiation. As discussed in the introduction, there has been significant debate about which of these fluxes plays a stronger role in maintaining the upper limit on SST. Results from the composite analysis indicate that the deep convective perturbations to the downwelling shortwave during the cool phase of the composite ocean hot spot are about -25 W m^{-2}, while the perturbations to the latent heat flux are only about -3 to -12 W m^{-2} (for reasonable choices of $L\rho C_E$). It should be stressed, however, that the data for assessing the evaporation flux anomalies (COADS) are not of high quality or well sampled. While these results suggest that shortwave cloud forcing is more important than evaporation in limiting the maximum SST in this context, they do not address whether these perturbations are strictly induced by the local increase in SST. As mentioned above, the local enhancements to convection can be initiated by MJO variability, variability that is internal to the atmosphere and not necessarily forced by the local SST. Even so, the coupling between the response of the SST and the effects of the MJO suggests an interesting avenue of feedback to the MJO. In the subsidence regions, the upper ocean absorbs significant energy that can then be used by the ensuing phase of enhanced convection.

Composite ocean conditions indicated that fairly rapid changes occur in the upper ocean in concert with the evolution of the atmosphere above. First, temperature anomalies associated with hot spot formation occur down to 200 m or more. These temperature anomalies are coincident with a 4–5-cm positive sea level height anomaly. Moreover, their magnitude and extent suggest that, in some cases, their formation and removal cannot be strictly attributed to surface heat flux changes but are also likely due to changes in internal ocean heat fluxes. Rather significant changes are also observed in the anomalous meridional and zonal velocity fields over the lifetime of the composite hot spot. For example, the change in anomalous wind stress resulting from the onset of westerly wind burst conditions (associated with the enhanced deep convection over the hot spot in the decay phase), along with the accompanying changes in sea level, can result in changes to zonal velocity anomalies on the order of 6 cm s^{-1} at 100 m, as well as near-surface meridional velocity changes of 1 cm s^{-1} or more. While the data available from this model analysis are not sufficient to address the degree internal ocean heat flux changes are responsible for the formation/decay of the ocean hot spots, it does offer a glimpse of the possible role the warm-pool ocean may be playing in this context and certainly establishes the likelihood that it is not behaving as a passive ocean mixed layer.

As mentioned above, the relatively cool conditions that persist during a La Niña period tend to inhibit the formation of ocean hot spots. Because of this, the overall background state of the composite ocean and atmosphere presented was biased in favor of El Niño conditions, even though most ocean hot spots occur in between the high-amplitude phases of ENSO. To determine how sensitive the composites, and thus the conclusions drawn from them, were to the inclusion of these El Niño time periods, the composites were recomputed after excluding El Niño months from the averages. As expected, the overall background state of these revised composites is tilted toward La Niña conditions. This included a change in the large-scale SST pattern from weak El Niño to weak La Niña conditions, a slight westward shift in the dominant convection anomalies in the western Pacific and Indian Oceans, a change in the sign of the Pacific wind stress and near-equatorial current anomalies, along with some significant changes in the large-scale atmospheric temperature and relative humidity anomalies. However, the character of the relationship between the convection and the SST in the region of hot spot formation/decay

did not change, nor did many of the relative changes associated the composite hot spot evolution. For example, both sets of composites showed relatively weaker (enhanced) low-level westerlies in the western Pacific during (after) the occurrence of the hot spot, even though the overall low-level wind anomalies were quite different between the two.

Excluding the El Niño time periods appeared to increase the importance of the downwelling surface shortwave (SW) during the month the hot spots occurred. While the cooling contributions from the SW and evaporation perturbations each appeared to decrease in the cool phase, their relative contributions remained about the same as before with the SW impact being greater. Overall, the above modifications in the composites did not appear to change the nature of the formation and decay mechanisms qualitatively, at least as far as the atmospheric component is concerned. The larger changes associated with the ocean composites indicate that the associated ocean conditions and processes are more sensitive to the interannual state of the system. This implies that the long memory of the ocean, in relation to the atmospheric forcing, does not always phase lock the same ocean and atmospheric processes during the formation and dissipation of an ocean hot spot.

The above results warrant some discussion regarding earlier studies. First, with respect to the thermostat hypothesis of RC, the composite results presented do indicate that the cooling effects due to cloudiness appear more important than those due to evaporation on limiting the very warm SSTs associated with hot spots in the western Pacific warm pool. However, there are indications that atmospheric variability uncoupled to the local SST (e.g., MJO) provide significant perturbations to the local convective environment that are important to both the formation and limiting mechanisms of very warm SST. Lau et al. (1994) argued that changes in the local convection, and thus cloudiness, are more directly linked to external forcing induced by the large-scale circulation rather than by the local SST, as would be implied by RC. The results presented here suggest, that at least at the intraseasonal time and space scales, this is often the case.

Finally, the notion of "hot patches" of SST invoked in the arguments of Wallace (1992) elicit a comparison with the composite "hot spots" presented and analyzed here. Following the argument of Wallace, hot patches will be subject to enhanced fluxes of latent heat. The observations presented here indicate that this is marginally the case (Fig. 8b), somewhat more so for the ENR composites (not shown). This enhanced latent heat flux is supposed to cool the SST and increase the frequency of convection over the hot patch. In fact, convection does increase over the region, but as mentioned above this is not necessarily motivated by the enhanced fluxes but may be brought on by anomalous vertical motion from remote, or uncoupled, atmospheric variability. In this stage, the SST does decrease, but the convective effects on surface shortwave appearing to be greater than on the latent heat flux. The heat carried upward by convection would then "heat up the troposphere not just over the local hot patches, but over the entire domain." This is generally supported by the composite pressure–latitude diagrams of temperature anomalies (Fig. 16) and the corresponding pressure–longitude diagrams (not shown). Therefore, the behavior of the hypothesized "hot patches" is somewhat similar to the observed "hot spots." However, the importance of perturbations to the surface shortwave budget and the effects of atmospheric variability uncoupled to the regions of high SST appear to play a more important role in the observed versus hypothesized cases.

It is worth emphasizing that the conclusions and inferences drawn from this study rely on the temporal resolution and quality of data used, with each dataset having at least one, and probably a number, of shortcomings. Examples include the HRC based on a subjective analysis of satellite data; the ISCCP and shortwave products only extend about 8 yr; the surface observations of humidity and wind speed are undersampled in many areas; and the model analysis fields are all based on sparse data in the Tropics and the assimilation systems that produced them have changed over time. While no one of these shortcomings is defensible, the intention here was to use as much of this historical data as possible to develop a coherent picture of the formation and decay mechanisms associated with very warm SSTs. In general, most of the variables showed considerable consistency among their composites and the processes these composites conveyed. Improvements to this study will come from the use of data with higher time resolution and longer records and, in particular, from the use of data derived from improved observation–model blending techniques [e.g., SST, shortwave, model reanalyses (Kalnay and Jenne 1991)].

While the aim of this study was to address the ocean and atmosphere processes responsible for limiting SST in general, it is hoped that the study's focus on the western Pacific warm pool will help to complement the results from the recent TOGA COARE and CEPEX field study programs. This study's application of long-term, historical data and large-scale composites that extend beyond the immediate domain of these program's field observations can help to augment and extend the results and inferences made from the observations obtained over the limited time periods of these programs. Investigation is currently underway to examine hot spot formation/decay in the northern Indian Ocean, where the coupling between the ocean and atmosphere is not expected to necessarily be the same. Future plans involve analyzing the ocean's role in this process in more detail, from observations as well as from coupled and forced ocean models.

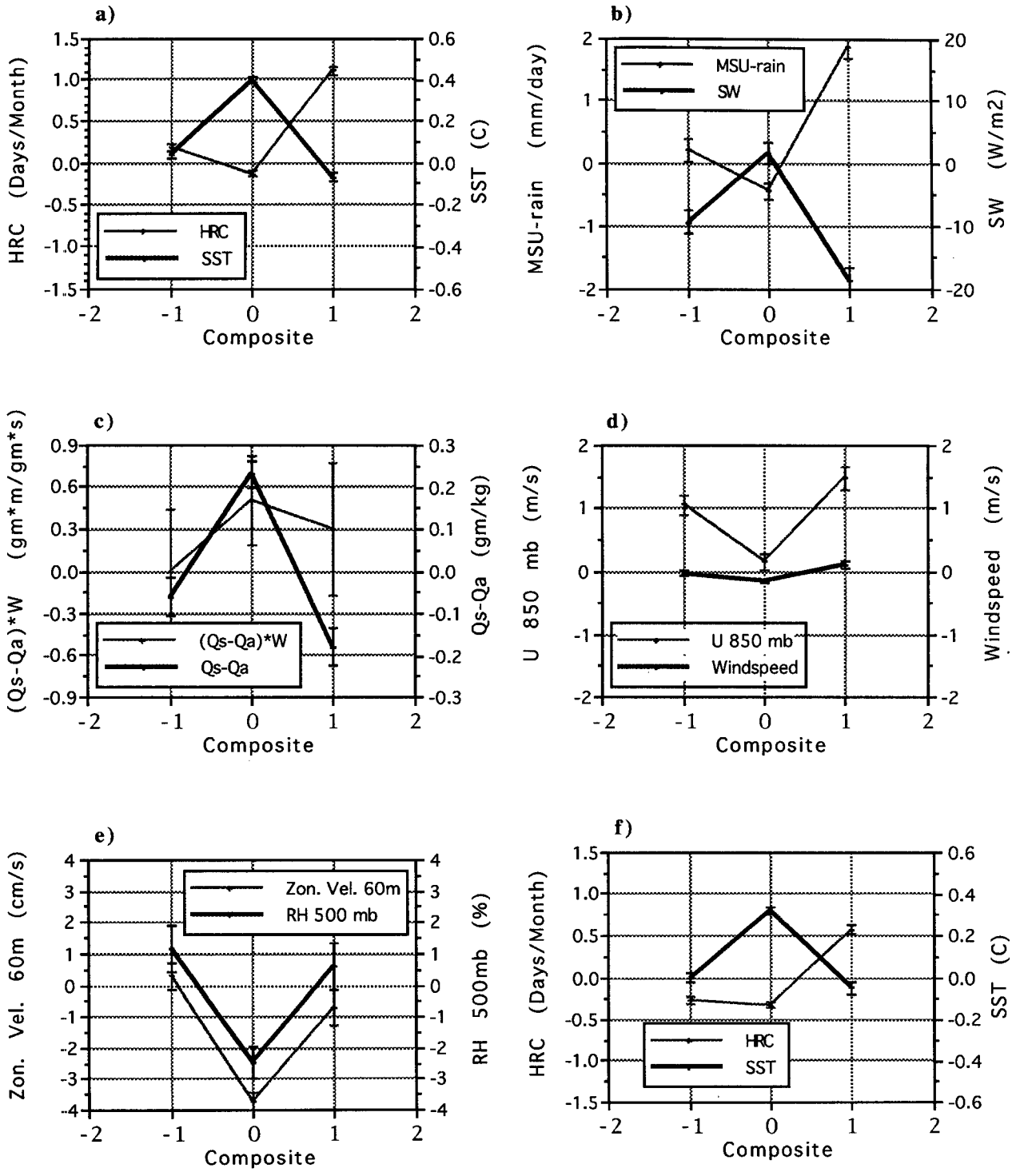

FIG. A1. Composite-to-composite changes in anomaly patterns averaged over the selection region. Error bars denote 95% confidence limits for the mean values. (a) HRC (thin; see Fig. 6), SST (thick; see Fig. 5); (b) SW (thick; see Fig. 10), MSU rainfall (thin; composite not shown); (c) $(Qs - Qa)$ (thick; see Fig. 8), $(Qs - Qa)W$ (thin; see Fig. 9); (d) surface wind speed (thick; see Fig. 7), 850-mb zonal wind speed (thin; see Fig. 13); (e) 500-mb relative humidity (thick; see Fig. 14), 60-m zonal current (thin; see Fig. 19); (f) HRC (thin; see Fig. 23), SST (thick; see Fig. 22) for ENR cases—see section 4f.

Acknowledgments. Support for this study was provided by the Climate Dynamics Program in the Atmospheric Sciences Division of the National Science Foundation under Grant ATM-9420833. The author would like to thank Catherine Gautier for helping to establish the study, providing the surface shortwave data, and for many useful discussions pertaining to the results. This study greatly benefited from many hours of discussion with Nick Graham over the WG article. The author would like to thank Minghua Zhang, as well as two anonymous reviewers, for many helpful comments and suggestions regarding the manuscript. The author would also like to thank Ming Ji for providing the NMC ocean analysis, J. Janowick for helpful discussions regarding the NMC analysis, Kevin Trenberth and Jeff Berry for providing the ECMWF analysis, Roy Spencer for providing the MSU rainfall data, Steve Worley and the NCAR Data Support Section for helping to provide the COADS data, Bob Cess and Danny Lu for providing the ERBE cloud-forcing data, John Horel for providing the OLR data, and the FSU Mesoscale Air–Sea Interaction Group for providing the pseudostress data. This study's analysis greatly benefited from the use of the TeraScan software analysis system, a product of SeaSpace Corporation, San Diego, California.

APPENDIX

Statistical Significance of Composite for Composite Changes

The plots in Fig. A1 illustrate the composite to composite changes for several of the analyzed quantities averaged over the selection region. Given are the mean quantities for each of the composites (−1, 0, +1), along with the error bars denoting 95% confidence limits on the means using the Student's t-test criteria. The number of points used in each mean comes from the number of "maps" used in each composite (number given at upper right-hand corner of each composite) multiplied by the number of points for that particular quantity's grid lying within the selection region.

REFERENCES

Anderson, S. A., and R. A. Weller, 1994: Moored observations of the variability and structure of temperature, salinity and velocity near the surface of the western Pacific warm pool during TOGA COARE. Summary Report of the TOGA COARE Int. Data Workshop, Toulouse, France, UCAR, 169 pp.

Arking, A., and D. Ziskin, 1994: Relationship between clouds and sea surface temperatures in the western tropical Pacific. *J. Climate,* **7,** 988–1000.

CEPEX, 1992: Central Equatorial Pacific Experiment: Experiment design. National Science Foundation Center for Clouds, Chemistry and Climate, University of California, San Diego, 56 pp.

Cess, R. D., and Coauthors, 1989: Interpretation of cloud–climate feedback as produced by 14 atmospheric general circulation models. *Science,* **245,** 513–516.

COADS, 1985: Comprehensive Ocean–Atmospheric Data Set, Release 1. Document available from Climate Research Program, NOAA Environmental Research Laboratory, Boulder, Colorado, 39 pp. plus suppls.

Emanuel, K. A., 1987: An air–sea interaction model of intraseasonal oscillations in the tropics. *J. Atmos. Sci.,* **44,** 2324–2340.

Fu, R., A. D. Del Genio, W. B. Rossow, and W. T. Liu, 1992: Cirrus-cloud thermostat for tropical sea surface temperatures tested using satellite data. *Nature,* **358,** 394–397.

Gadgil, S., P. V. Joseph, and N. V. Joshi, 1984: Ocean–atmosphere coupling over monsoon regions. *Nature,* **312,** 141–143.

Garcia, O., 1985: Atlas of highly reflective clouds for the global tropics: 1971–1983. U.S. Department of Commerce, NOAA, Environmental Research Lab., Boulder, CO, 365 pp.

Gautier, C., G. Diak, and S. Masse, 1980. A simple physical model to estimate incident solar radiation at the surface from GOES satellite data. *J. Climate Appl. Meteor.,* **19,** 1005–1012.

Graham, N. E., and T. P. Barnett, 1987: Sea surface temperature, surface wind divergence, and convection over tropical oceans. *Science,* **238,** 657–659.

Gruber, A., and A. F. Krueger, 1984: The status of the NOAA outgoing longwave radiation data set. *Bull. Amer. Meteor. Soc.,* **65,** 958–962.

Hartmann, D. L., and M. Michelsen, 1993: Large-scale effects on the regulation of tropical sea surface temperature. *J. Climate,* **6,** 2049–2062.

Hayes, S. P., L. J. Magnum, J. Picaut, A. Sumi, and K. Takeuchi, 1991: TOGA-TAO: A moored array for real-time measurements in the tropical Pacific Ocean. *Bull. Amer. Meteor. Soc.,* **72,** 339–347.

Hendon, H. H., and M. L. Salby, 1994: The life cycle of the Madden–Julian oscillation. *J. Atmos. Sci.,* **51,** 2225–2237.

Horel, J., and A. G. Cornejo-Garrido, 1986: Convection along the coast of northern Peru during 1986: Spatial and temporal variation of clouds and rainfall. *Mon. Wea. Rev.,* **114,** 2091–2105.

Ji, M., A. Leetma, and J. Derber, 1995: An ocean analysis system for climate studies. *Mon. Wea. Rev.,* **123,** 460–481.

Kalnay, E., and R. Jenne, 1991: Summary of the NMC/NCAR Reanalysis Workshop of April 1991. Meeting review. *Bull. Amer. Meteor. Soc.,* **72,** 1897.

Krueger, A. F., and T. I. Gray Jr., 1969: Long-term variations in equatorial circulation and rainfall. *Mon. Wea. Rev.,* **97,** 700–711.

Lau, K. M., and P. H. Chan, 1985: Aspects of the 40–50 day oscillation during the northern winter as inferred from outgoing longwave radiation. *Mon. Wea. Rev.,* **113,** 1889–1909.

——, and ——, 1988: Intraseasonal and interannual variations of tropical convection: A possible link between the 40–50 day oscillation and ENSO? *J. Atmos. Sci.,* **45,** 506–521.

——, C. H. Sui, M. D. Chou, and W. K. Tau, 1994: An inquiry into the cirrus-cloud thermostat effect for tropical sea surface temperature. *Geophys. Res. Let.,* **21,** 1157–1160.

Legler, D. M., I. M. Navon, and J. J. O'Brien, 1989: Objective analysis of pseudostress over the Indian Ocean using a direct-minimization approach. *Mon. Wea. Rev.,* **117,** 709–720.

Liebmann, B., and D. L. Hartmann, 1982: Interannual variations of outgoing IR associated with tropical circulation changes during 1974–1978. *J. Atmos. Sci.,* **39,** 1153–1162.

Lindzen, R. S., 1990: Some coolness concerning global warming. *Bull. Amer. Meteor. Soc.,* **71,** 288–299.

Liu, W. T., A. Zhang, and J. K. B. Bishop, 1994: Evaporation and solar irradiance as regulators of sea surface temperature in annual and interannual changes. *J. Geophys. Res.,* **99,** 12 623–12 637.

Madden, R., and P. R. Julian, 1971: Detection of a 40–50 day oscillation in the zonal wind in the tropical Pacific. *J. Atmos. Sci.,* **28,** 702–708.

Manabe, S., and R. T. Wetherald, 1980: On the distribution of climate change resulting from an increase in CO_2 content of the atmosphere. *J. Atmos. Sci.,* **37,** 99–118.

McPhaden, M. J., 1993: TOGA–TAO and the 1991–93 El Nino–Southern Oscillation event. *Oceanography,* **6,** 36–44.

Neelin, J. D., and J.-Y. Yu, 1993. Modes of tropical variability under convective adjustment and the Madden–Julian oscillation. Part I: Analytical results. *J. Atmos. Sci.*, **51,** 1876–1894.

Newell, R. E., 1979: Climate and the ocean., *Amer. Sci.*, **67,** 405–416.

Philander, S. G., 1991: *El Nino, La Nina, and the Southern Oscillation.* Academic Press, 293 pp.

Priestley, C. H. B., 1966: The limitation of temperature by evaporation in hot climates. *Agric. Meteor.*, **3,** 241–246.

Ramanathan, V., and W. Collins, 1991: Thermodynamic regulation of ocean warming by cirrus clouds deduced from observations of the 1987 El Nino. *Nature,* **351,** 27–32.

Rasmusson, E. M., and J. M. Wallace, 1983: Meteorological aspects of the El Nino/Southern Oscillation. *Science,* **222,** 1195–1202.

Raval, A., and V. Ramanathan, 1989: Observational determination of the greenhouse effect. *Nature,* **342,** 758–761.

Reynolds, R. W., 1988: A real-time global sea surface temperature analysis. *J. Climate,* **1,** 75–86.

Rossow, W. B., and R. A. Schiffer, 1991: ISCCP Cloud Data Products. *Bull. Amer. Meteor. Soc.,* **72,** 2–20.

Salby, M. L., and H. H. Hendon, 1994: Intraseasonal behavior of clouds, temperature, and motion in the Tropics. *J. Atmos. Sci.,* **51,** 2207–2224.

Schlesinger, M. E., and J. F. B. Mitchell, 1987: Climate model simulations of the equilibrium climate response to increased carbon dioxide. *Rev. Geophys.,* **25,** 760–798.

Shriver, J. F., and J. J. O'Brien, 1993: Interdecadal variability of the equatorial Pacific Ocean and atmosphere: 1930–1989. Mesoscale Air–Sea Interaction Group Tech. Rep.

Somerville, R. C. J., and L. A. Remer, 1984: Cloud optical thickness feedbacks in the CO_2 climate problem. *J. Geophys. Res.,* **89,** 9688–9672.

Spencer, R. W., 1993: Global oceanic precipitation from the MSU during 1979–91 and comparisons to other climatologies. *J. Climate,* **6,** 1301–1326.

Stephens, G. L., and T. J. Greenwald, 1991: The earth's radiation budget and its relation to atmospheric hydrology. Part 1: Observations of the clear sky greenhouse effect. *J. Geophys. Res.,* **96,** 15 311–15 324.

TOGA COARE, 1991: Tropical Ocean Global Atmosphere: Coupled Ocean Atmosphere Response Experiment. Experiment Design. TOGA COARE Projects Office, University Corporation of Atmospheric Research, Boulder, CO, 90 pp.

Trenberth, K. E., and J. G. Olson, 1988: An evaluation and intercomparison of global analysis from NMC and ECMWF. *Bull. Amer. Meteor. Soc.,* **69,** 1047–1057.

Waliser, D. E., and C. Gautier, 1993: A global climatology of the ITCZ. *J. Climate,* **6,** 2162–2174.

——, and N. E. Graham, 1993: Convective cloud systems and warm-pool SSTs: Coupled interactions and self-regulation. *J. Geophys. Res.,* **98**(D7), 12 881–12 893.

——, ——, and C. Gautier, 1993: Comparison of the highly reflective cloud and Outgoing Longwave Radiation datasets for use in estimating tropical deep convection. *J. Climate,* **6,** 331–353.

——, B. Blanke, J. D. Neelin, and C. G. Gautier, 1994: Shortwave feedbacks and ENSO: Forced ocean and coupled ocean–atmosphere experiments. *J. Geophys. Res.* in press.

Wallace, J., 1992: Effect of deep convection on the regulation of tropical sea surface temperature. *Nature,* **357,** 230–231.

Wang, T., 1994: Satellite-derived long term net solar radiation over the global ocean surface: Its relationship to low frequency SST variation and El Nino. M.S. thesis, University of California, Santa Barbara.

Weickmann, K. M., 1983: Intraseasonal circulation and outgoing longwave radiation modes during Northern Hemisphere winter. *Mon. Wea. Rev.,* **111,** 1838–1858.

Weller, R. A., and S. A. Anderson, 1995: Surface meteorology and air–sea fluxes in the western equatorial Pacific during the TOGA Coupled Ocean Atmosphere Response Experiment. *J. Geophys. Res.,* in preparation.

Young, G. S., D. V. Ledvina, and C. W. Fairall, 1992: Influence of precipitating convection on the surface energy budget observed during a TOGA pilot cruise in the tropical western Pacific Ocean. *J. Geophys. Res. (Oceans),* **97,** 9595–9603.